Mon. Not. R. Astron. Soc. **421,** 635–650 (2012) doi:10.1111/j.1365-2966.2011.20341.x

Mapping the galaxy NGC 4486 (M87) through its globular cluster system

Juan C. Forte,[1,2]★ E. Irene Vega[1,2] and Favio Faifer[1,2,3]

[1] *Facultad de Ciencias Astronómicas y Geofísicas, Universidad Nacional de La Plata, La Plata, Argentina*
[2] *Consejo Nacional de Investigaciones Científicas y Técnicas, Argentina*
[3] *Instituto de Astrofisica de La Plata, La Plata, Argentina*

Accepted 2011 December 6. Received 2011 November 29; in original form 2011 October 4

ABSTRACT

As shown in previous works, globular clusters (GCs) can be used to trace the overall structure of the diffuse stellar populations in early-type galaxies if the number of clusters per unit stellar mass depends on metallicity. In this paper we further test this assumption in the galaxy NGC 4486 (M87) by combining several data sources. The results show that GCs allow the mapping of the galaxy in terms of the surface brightness profile, integrated colour gradient, chemical abundance and mass-to-luminosity ratios up to 1000 arcsec (or 80.4 kpc) from its centre (i.e. some 10 effective radii). The analysis indicates the presence of a dominant high-metallicity bulge associated with the red globulars, whose ellipticity increases outwards, and of a more flattened low-metallicity halo connected with the blue globulars. The chemical abundance gradient of the composite stellar population is remarkably similar to that inferred from X-ray observations of hot gas. The mass–metallicity spectrum of the stellar population can, in principle, be understood in terms of inhomogeneous enrichment models. In turn, the distribution of the bluest GCs, and lowest metallicity halo stars, has an intriguing similarity with that of dark matter, a feature shared with NGC 1399. Also, in these two galaxies, the number of blue GCs per dark mass unit is identical within the errors, $\approx 1.0(\pm 0.3) \times 10^{-9}$. The total stellar mass derived for NGC 4486 is $6.8(\pm 1.1) \times 10^{11}\,\mathrm{M}_{\odot}$ with a baryonic mass fraction $f_{\mathrm{b}} = 0.08(\pm 0.01)$.

Key words: globular clusters: general – galaxies: haloes – galaxies: star clusters: general.

1 INTRODUCTION

The potential of globular clusters (GCs) as tracers of early events in the life of galaxies has been frequently emphasized in the literature. The idea has roots in Eggen, Lynden Bell & Sandage (1962) and Searle & Zinn (1978) and a landscape of the different issues within that context is given, for example, in Brodie & Strader (2006). The theoretical aspects of the problem have been addressed in an effort to define its cosmological background (e.g. Beasley et al. 2002; Bekki et al. 2008; Muratov & Gnedin 2010).

However, as noted by Kissler-Patig (2009), and also see Spitler (2010), some important aspects remain as open questions. Among them, the striking differences that are observed between the metallicity distribution function (MDF) of the CGs, usually bimodal, and that of field stars as observed in resolved galaxies. In this last case the MDFs are predominantly broad, asymmetric and exhibit a low-metallicity tail (e.g. Durrell, Harris & Pritchet 2001; Harris & Harris 2002; Rejkuba et al. 2005; Rejkuba et al. 2011).

Differences and similarities between GCs and the underlying stellar populations have been pointed out in the past. For example, Forte, Strom & Strom (1981) and Strom et al. (1981) found that GCs appear significantly bluer than the stellar haloes at all galactocentric distances in four Virgo ellipticals.

These comparisons should take into account, however, that the CG statistics are 'number weighted' while halo colours are, naturally, 'luminosity weighted'. Thus, a coincidence between GC and stellar halo colours would be expected only if each GC formed along a given diffuse stellar mass on a constant luminosity basis. This fact is frequently ignored in the literature.

A possible quantitative connection between the features of GCs and field stars suggests that clusters are born during major star-forming episodes and assumes that the number of clusters per diffuse stellar mass varies exponentially with chemical abundance. This connection is consistent with the variation of the GC's specific frequency S_n with chemical abundance (Harris & Harris 2002), and allows the recovery of both the luminosity profile and colour gradient in a galaxy as the result of a multi-metallicity stellar population.

A first approach along these lines was presented in Forte, Faifer & Geisler (2007) (hereafter FFG07). More consequences of that idea were discussed in Forte, Vega & Faifer (2009) (hereafter FVF09) who performed an analysis of 69 galaxies within the Virgo Advanced Camera Survey (ACS) (see Ferrarese et al. 2006; Peng et al. 2008).

★E-mail: forte@fcaglp.unlp.edu.ar

FVF09 also find that globular cluster systems (GCS) in Virgo galaxies with stellar masses below $M_* \approx 10^{11}$ M$_\odot$ lie on plane defined (in a 3D logarithmic space) by GC formation efficiency (number of GCs per unit stellar mass), total stellar mass and projected stellar mass density. NGC 4486, and other bright Virgo ellipticals, lies well outside this plane, probably reflecting the effects of past merger events.

In this paper we revise the case of NGC 4486 (M87), taking advantage of a number of photometric works (Tamura et al. 2006; Harris 2009; Jordán et al. 2009) that, combined, allow an analysis on an angular scale of ≈1000 arcsec.

An important assumption of the analysis is that GCs and field stars are mostly coeval or formed within a narrow period of time. Arguments in support of this hypothesis can be found, for example, in Spitler (2010) and references therein. In particular, a direct estimate of the age of the halo of the galaxy NGC 3923, as well as of its associated GCs, was presented by Norris et al. (2008) using Gemini spectra (taken with the Multi Optical Spectrometer (MOS)) and Lick indices. These results also indicate an old age (about 12 Gyr) for both stars and GCs (see Beasley et al. 2008 for the case of NGC 5128).

More arguments in favour of old ages and multi-metallicity spectra for the dominant stellar populations in elliptical galaxies stand on the analysis of their integrated colours as discussed in Schombert & Rakos (2009).

Several papers, on the other hand, deal with the surface brightness profile of NGC 4486. In this work we adopt the blue band (Johnson system) surface brightness profile presented by Caon, Capaccioli & Rampazzo (1990). All these works denote the existence of a flattened cD halo (already detected by Arp & Bertola 1971), traced to very low luminosity levels in Mihos et al. (2005). More recently, Rudick et al. (2010) find that the $(B - V)$ colour gradient of the galaxy has a logarithmic dependence along the semimajor axis over an angular range of (at least) 1000 arcsec (i.e. approximately 10 effective radii). This corresponds to 80.1 kpc for a distance modulus $(Vo - M_v) = 31.1$, or 16.5 Mpc (Tonry et al. 2001), adopted in this work.

This paper is organized as follows. Section 2 presents an improved version of the GC integrated colours versus metallicity relation given in FFG07 and the connection between chemical abundance Z (in solar units hereafter) and the cluster integrated colours, including an attempt to model the so-called 'blue tilt'. Section 3 explains the assumed link between GCs and field stars. Section 4 describes the fit of the GC colour histograms within the inner 300 arcsec along the galaxy semimajor axis, aiming at determining the number of clusters belonging to the blue or red sub-population as well as their respective chemical scalelengths. A discussion of the large angular scale features of the galaxy, including the shape of the surface brightness profile, colour gradient, stellar metallicity function and stellar-mass-to-luminosity ratios, is given in Section 5. The inferred halo, bulge and total stellar masses, and a comparison with the dark matter content, are presented in Section 6. Finally, the GCs formation efficiencies for both the blue and red GCs and the conclusions of this paper are included in Sections 7 and 8, respectively.

2 THE GLOBULAR CLUSTERS COLOUR DISTRIBUTION

In their analysis of the GCS systems associated with Virgo ellipticals, Peng et al. (2006) present non-parametric fits of the CG colour histograms. In this paper we adopt a different approach that seeks the determination of the chemical abundance scales as well as the fraction of clusters in each population, on the basis of a Monte Carlo simulation.

As discussed in FFG07, the simplest function that links the chemical abundance Z with the integrated $(C - T_1)_o$ colours through the empirical calibration, and within the inherent statistical noise of the GC counts, is

$$\mathrm{d}N(Z)/\mathrm{d}Z \approx \exp(-(Z - Zi)/Z_\mathrm{s}) \quad (1)$$

where Zi is a pedestal abundance and Z_s is the characteristic abundance scalelength of each GC sub-population.

The modelling of the GCs colour bimodality is then similar to that given in FFG07. First, a 'seed' globular is randomly generated with a given Z governed by the Z_s parameter. The synthetic integrated colours were in turn obtained from the empirical colour metallicity calibration and adding Gaussian observational errors. A colour excess $E(B - V) = 0.02$ from Schlegel, Finkbeiner & Davis (1998), which transforms to $E(C - T_1) = 0.04$, was also added to the intrinsic $(C - T_1)_o$ colours in order to match the FFG07 photometry. T_1 magnitudes were also generated for each cluster adopting a GC Gaussian luminosity function with a turn over at $T_1 = 23.2$ and characterized by a dispersion $\sigma(T_1) = 1.60$ mag. A detailed discussion of the behaviour of this parameter for the Virgo ACS galaxies is given in Villegas et al. (2010).

The shape of the empirical colour–metallicity relation requires a GC bimodal metallicity distribution in order to match the observed colour bimodality defined in terms of the so-called blue and red GCs (for which we adopt upper chemical abundance values $Z = \mathrm{Z}_\odot$ and $Z = 3.5\,\mathrm{Z}_\odot$, respectively). Previous, and more recent, arguments in favour of bimodal GC metallicity distributions can be found, for example, in Alves-Brito et al. (2011) (however, see Yoon et al. 2011 for a different interpretation of the colour bimodality).

FFG07 presented an empirical colour–metallicity relation based on 100 Milky Way (MW) GCs with $(C - T_1)$ Washington system colours and 98 extragalactic GCs with $(g' - i')$ colours in the (modified) Gunn system. In turn, Moyano Loyola, Faifer & Forte (2010) derived an improved version of that calibration:

$$(C - T_1)_o = 0.91(\pm0.15) + 0.06(\pm0.02)([\mathrm{Fe/H}]_{zw} + 3.70(\pm0.87))^2 \quad (2)$$

where $[\mathrm{Fe/H}]_{zw}$ are metallicities on the Zinn & West (1984) scale. The improvement comes from a better determination of the relation used to transform $(g' - i')_o$ to $(C - T_1)_o$:

$$(C - T_1)_o = 1.72(\pm0.04)(g' - i')_o - 0.07(\pm0.06) \quad (3)$$

obtained by observing a reference field in NGC 4486 with Gemini/MOS (Forte et al., in preparation) with GC candidates observed in both photometric systems. In turn, from FFG07 and Jordán et al. (2009):

$$(C - T_1)_o = 1.26(\pm0.04)(g - z)_{o,\mathrm{ACS}} + 0.01(\pm0.05). \quad (4)$$

Other colour–colour relations used in this work are

$$(B - V)_o = 0.51(\pm0.03)(C - T_1)_o + 0.06(\pm0.04) \quad (5)$$

$$(B - R)_o = 0.70(\pm0.06)(C - T_1)_o + 0.27(\pm0.07) \quad (6)$$

$$(V - I)_o = 0.50(\pm0.06)(C - T_1)_o + 0.32(\pm0.07) \quad (7)$$

derived from observations of galactic globulars (see also Forbes & Forte 2001) and can be used to transform the relation given in equation (2) to other colours.

A similar calibration based on 40 MW GCs, and presented in Sinnott et al. (2011), shows very good agreement with ours in the range defined between [Fe/H] −2.5 and −0.5. At higher metallicities, their calibration (that includes three MW GCs, compared with 26 GCs that define equation 2) becomes steeper and leads to $(C - T_1)$ colours redder by 0.15 mag at [Fe/H] = 0.0.

An analysis of the colour residuals from our adopted calibration as a function of the GC ages, determined from colour–magnitude diagrams for the MW GCs, or from Lick indices for the extragalactic globulars, reveals no systematic trends. The empirical calibration, then, corresponds to the mean age of the MW GCs, which we assume as 12 Gyr.

For any other age τ (in Gyr) the colour transforms to

$$(C - T_1)_\tau = (C - T_1)_o + \Delta(C - T_1) \tag{8}$$

with

$$\Delta(C - T_1) = (\tau - 12.0)\mathrm{d}(C - T_1)/\mathrm{d}\tau \tag{9}$$

where the term $\mathrm{d}(C - T_1)/\mathrm{d}\tau$ can be approximated, for ages between 8 and 15 Gyr, as

$$\mathrm{d}(C - T_1)/\mathrm{d}\tau = 0.02 + 5.3 \times 10^{-3}[\mathrm{Fe/H}]_{zw} \tag{10}$$

derived from the single stellar population models by Bruzual & Charlot (2003).

On the other hand, Mendel, Proctor & Forbes (2007) connect the $[\mathrm{Fe/H}]_{zw}$ metallicity scale with the total chemical abundance of the Thomas, Maraston & Korn (2004) models through:

$$[\mathrm{Z/H}] = [\mathrm{Fe/H}]_{zw} + 0.131. \tag{11}$$

The GCs colour–magnitude diagram for NGC 4486 shows the so-called 'blue tilt' (Peng et al. 2009, and references therein), a feature explained in FFG07 as an increase of the *Zi* parameter with the GC brightness and mass. Alternative views about the interpretation of the blue tilt, and the role of chemical pre- and/or self-enrichment, are given in Strader & Smith (2008) and Bailin & Harris (2009).

A linear relation between colours and GC magnitudes was adopted in FFG07 to describe the tilt. However, a new analysis rather suggests a non-linear trend (see also the colour–magnitude diagrams presented by Harris 2009):

$$(C - T_1)_t = 21.67\, T_1^{-0.95} \tag{12}$$

where $(C - T_1)_t$ and T_1 are (reddening corrected) colours and magnitudes that define the tilt shape. At a given T_1, the $(C - T_1)_t$ colour leads to a metallicity defined through the empirical colour–metallicity relation, $[\mathrm{Fe/H}]_t$, and then to a $[\mathrm{Z/H}]_t$ from the Mendel et al. relation:

$$[\mathrm{Z/H}]_t = [\mathrm{Fe/H}]_t + 0.131. \tag{13}$$

In this paper, we attempt modelling the chemical variation associated with the tilt by defining:

$$Zi = Zoi + \Delta Z, \tag{14}$$

where *Zoi* is a fit parameter (the lowest chemical abundance for a given GC sample), and ΔZ is given by

$$\Delta Z = 10^{[\mathrm{Z/H}]_t} - 0.092. \tag{15}$$

This procedure leads to values that range from $\Delta Z = 0.06$ at $T_1 = 19.0$ mag, corresponding to the brightest objects, to $\Delta Z = 0.0$ at $T_1 = 23.2$ mag, the turn-over of the GCs integrated luminosity function, where the tilt seems to disappear.

3 THE GLOBULAR CLUSTERS–FIELD STARS CONNECTION

As shown in several papers, the metallicity distributions of GCs and resolved field stars are noticeably different [see e.g. Durrell et al. (2001) for M31 or Rejkuba et al. (2011) for NGC 5128]. The tentative link between these systems, explored in FFG07 and FFG09, comes from the fact that both the number N of GCs per unit stellar mass (e.g. Miller & Lotz 2007) and the metallicity of a galaxy (Tremonti et al. 2004) can be approximated as power laws of the stellar galaxy mass. Combining these relations, and adding an explicit dependence with chemical abundance, leads to

$$\mathrm{d}N(Z)/\mathrm{d}M_*(Z) = \gamma \exp(-\delta[\mathrm{Z/H}]). \tag{16}$$

This equation connects $\mathrm{d}N(Z)$, derived from the GC colour histograms, to a (assumed coeval) diffuse stellar mass element $\mathrm{d}M_*(Z)$, whose mass-to-luminosity ratio and colour solely depend on chemical abundance.

Then, the knowledge of the projected GC areal density at a given galactocentric radius allows the fit of the colour and surface brightness of the galaxy by iterating the δ and γ parameters, and integrating in the chemical abundance domain covered by the GCs. Equation (16) implies that the integrated colours, composite (M/L) ratios and mean chemical abundances (mass or luminosity weighted) are governed by δ since this parameter regulates the relative masses of stars associated with GC with different chemical abundances.

As in FF07 and FVF09, the B luminosity associated with $M_*(Z)$ was obtained from

$$(M/L)_B = 3.71 + ([\mathrm{Z/H}] + 2.0)^{2.5} \tag{17}$$

which gives a good approximation to the mass to B luminosity ratios, given by Worthey (1994) for a Salpeter stellar mass function. An idea about the uncertainty of this relation comes from a comparison with other models. For example, the Maraston (2004) models show an agreement within 10 per cent with Worthey's although, at the lowest chemical abundance, this last author gives ratios ≈24 per cent larger. Other source of uncertainty is connected with the assumed stellar mass function. The adoption of a Chabrier (2003) function leads to stellar masses systematically smaller by a factor of 0.55.

4 NGC 4486: THE INNER 300 ARCSEC (24.1 KPC)

In this section we discuss the inner 300 arcsec along the semimajor axis of the galaxy, where the photometric works by Jordán et al. (2009) and FFG07 give a complete areal coverage for objects brighter than the GCs turn-over. At this magnitude level we estimate a background contamination of about one object per square arcmin, which agrees with the value given by Harris (2009), after taking into account the slightly different limiting magnitude in both works.

In particular, for the region discussed in this section, the total expected background contamination should be below 5 per cent, then minimizing the effects of these objects on the colour histograms of the GC candidates.

In contrast with FFG07, where single scale parameters Z_{SB} and Z_{SR} were adopted to characterize either the blue or the red GC population, we performed distinct fits within elliptical annuli (30 arcsec wide) following the ellipticity variation of the galaxy halo in an attempt to detect chemical abundance gradients.

An analysis of all the colour histograms shows a small asymmetry in the sense that GCs to the NE of the semimajor axis of the galaxy seem slightly redder [by ≈0.015 in $(C - T_1)$] than those to the SW

Table 1. Fit parameters for the GC colour histograms, colours and chemical abundances for GCs and NGC 4486.

$\bar{a}$ (arcsec)	ϵ	$N_{\rm blue}$	$Z_{\rm SB}$	Z_{oiB}	[Z/H] BGC	N_R	$Z_{\rm SR}$	Z_{oiR}	[Z/H] RGC	$(B-R)$ GCs	$(B-R)$ Galaxy	$[Z/H]_{\rm M}$ Galaxy	$[Z/H]_{\rm L}$ Galaxy
18.7	0.03	55	0.085	10^{-3}	−1.09	81	1.45	0.10	−0.02	1.40	1.56	0.21	0.12
45.5	0.07	105	0.030	10^{-3}	−1.41	185	1.35	0.05	−0.07	1.37	1.52	0.19	0.11
74.7	0.10	140	0.030	10^{-3}	−1.41	140	1.35	0.05	−0.07	1.33	1.50	0.18	0.09
105.3	0.13	150	0.035	10^{-3}	−1.37	159	1.35	0.10	−0.04	1.33	1.48	0.16	0.06
135.2	0.16	119	0.035	10^{-3}	−1.37	119	1.20	0.10	−0.06	1.32	1.47	0.14	0.04
165.5	0.18	120	0.020	10^{-3}	−1.52	130	0.80	0.05	−0.21	1.27	1.46	0.07	−0.03
194.4	0.21	139	0.020	10^{-3}	−1.52	118	0.85	0.05	−0.19	1.28	1.46	0.09	−0.02
224.5	0.23	130	0.025	10^{-3}	−1.46	103	0.95	0.05	−0.16	1.26	1.45	0.08	0.00
255.4	0.25	140	0.020	10^{-3}	−1.52	95	0.85	0.05	−0.20	1.24	1.45	0.08	−0.04
284.7	0.27	120	0.020	10^{-3}	−1.52	85	0.80	0.05	−0.21	1.25	1.44	0.06	−0.06

Column 1: mean $\bar{a}$ semimajor axis of the annulus; Column 2: mean ellipticity; Column 3: number of blue GCs; Column 4: chemical scalelength for the blue GCs; Column 5: initial chemical abundance for blue GCs; Column 6: mean chemical abundance for the blue GCs; Column 7: number of red GCs; Column 8: chemical scalelength for red GCs; Column 9: initial chemical abundance for red GCs; Column 10: mean chemical abundance for red GCs; Column 11: mean $(B-R)$ colours for the whole GC population; Column 12: integrated $(B-R)$ colour of the galaxy; Column 13: mean chemical abundance for the galaxy (mass weighted); Column 14: mean chemical abundance for the galaxy (B luminosity weighted).

of that axis, and may indicate differential reddening. Besides, the three outermost annuli show a bump at $(C-T_1) \approx 0.95$ (see the Appendix).

The nature of these objects (around 50 in total) remains unclear although we noticed that they appear mostly to the NE of the galaxy major semi-axis and without any obvious concentration towards the centre of the galaxy. As a tentative explanation, they might be foreground MW stars connected with the so-called 'Virgo overdensity' (see e.g. Lee et al. 2010).

The GC colour histograms were fit by iterating the Z_{oi} and $Z_{\rm s}$ parameters as well as the number of clusters of each sub-population and minimizing the 'quality fit' parameter defined by Côté, Marzke & West (1998). These values are listed in Table 1. Typical errors of the $Z_{\rm SB}$ and $Z_{\rm SR}$ parameters are ± 0.005 and ± 0.05, respectively.

The observed and model GC colour distributions are displayed in the Appendix (Figs A1– A3), both in discrete bins and smoothed histograms.

The GC colour histograms corresponding to regions defined between $a = 0$ to 90 arcsec and $a = 90$ to 300 arcsec are depicted in Figs 1 and 2. These diagrams also display the composite model colour histograms obtained by combining the individual fits listed in Table 1. This table shows a decrease of the GC's chemical scales $Z_{\rm SB}$ and $Z_{\rm SR}$ along the semimajor axis of the galaxy, and also a difference in the sense that red GCs require higher values of the initial abundances Z_{oi}, compared to those of the blue GCs.

The ΔZ component of the Zi parameter (Section 2) was also included in the colour modelling of the red GCs. However, their large chemical abundance scalelength, compared with the ΔZ parameter, makes the tilt effect practically undetectable for these clusters.

The $(B-R)$ colour gradient of the galaxy and the mean integrated colours of the whole cluster population are shown in Fig. 3. This last gradient is steeper than that of the galaxy, an effect noted, for example, by Liu et al. (2011). We stress that both gradients are sensitive to eventual chemical gradients but, while the first one reflects the luminosity weighted contribution of the different diffuse stellar populations, the GC gradient is also sensitive to the change of the relative number of blue to red clusters along the galaxy major axis.

The galaxy gradient in the last figure is based on the *BVRI* data discussed by Michard (2000). This author determined the sky level in each photometric band through an iterative procedure that led to consistent *'nice logarithmic gradients'*.

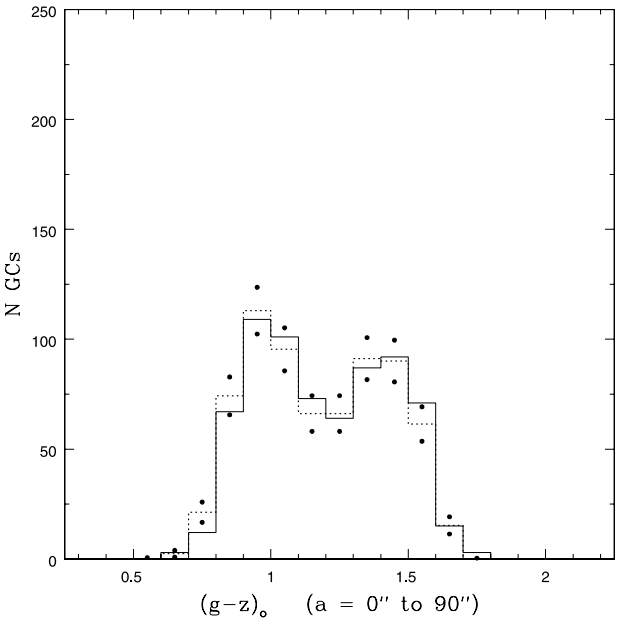

Figure 1. $(g-z)_o$ colour histogram for 706 GC candidates within a semimajor axis $a = 90$ arcsec (7.2 kpc), where the areal coverage given in Jordán et al. (2009) is complete. The dotted line shows a composite model based on the parameters listed in Table 1. Dots indicate the statistical uncertainty of the model within each 0.1 mag bin.

Transforming the Michard's colour gradients to $(B-R)$, through the colour–colour relations given in Section 2, leads to a mean gradient:

$$\Delta(B-R)/\Delta\log(a) = -0.11 \pm 0.02.$$

The δ parameter that fits the $(B-R)$ colour of the galaxy within each annular region was determined using the GCs parameters listed in Table 1. In turn, the γ parameter was obtained in such a way that the model B magnitude agreed with that obtained by integrating the Caon et al. (1990) profile within the inner and outer boundaries of each annulus.

The run of the δ and γ parameters along semimajor axis of the galaxy are displayed in Figs 4 and 5, respectively. The first one shows a mean value of 1.80 with an rms of ± 0.05. In contrast, γ rises in a monotonic way until reaching a value of about

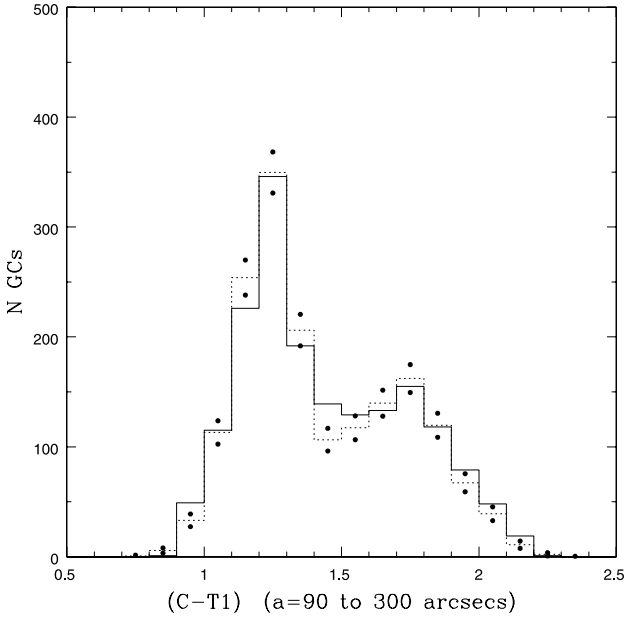

Figure 2. $(C - T_1)$ colour histogram for 1727 GC candidates between $a = 90$ and 300 arcsec (7.2 to 24.1 kpc) where the areal coverage of the photometry by Forte et al. (2007) is complete. Dotted lines and dots have the same meaning as in the previous figure.

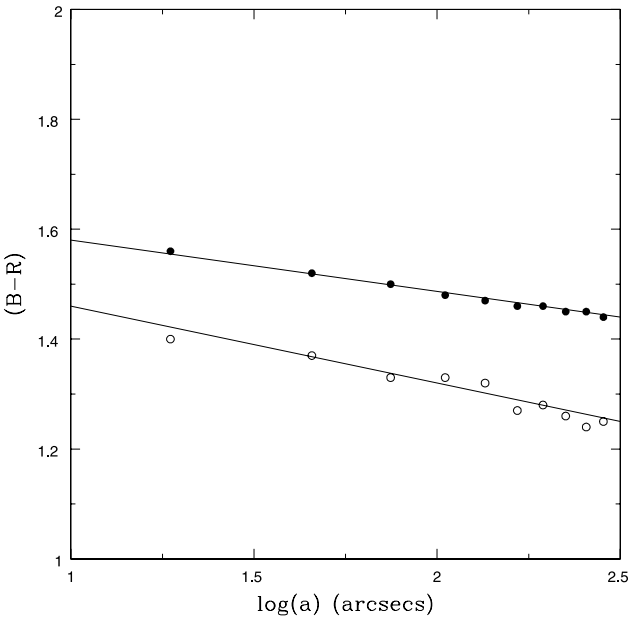

Figure 3. Logarithmic $(B - R)$ colour gradients along the NGC 4486 semimajor axis (within 30 arcsec wide elliptical annuli). Galaxy: filled dots. GCs (mean values): open dots.

0.55×10^{-8} at $a \approx 250$ arcsec. This trend indicates an increasing number of GCs per diffuse stellar mass, and may be explained as the result of dynamical destruction/erosion effects, which become less important with increasing galactocentric radius (see e.g. Capuzzo-Dolcetta & Mastrobuono-Battisti 2009 and references therein).

Table 1 also includes the mean chemical abundance (number weighted) for the blue and red GCs, and the mean chemical abundance (mass and luminosity weighted) of the inferred composite stellar population. Linear least-squares fit to the blue GC abundances (with a in arcsec) yields:

$$[\mathrm{Z/H}] = -0.17(\pm0.07)\log(a) - 1.08(\pm0.15) \quad (18)$$

and for the red GCs:

$$[\mathrm{Z/H}] = -0.17(\pm0.05)\log(a) + 0.22(\pm0.09) \quad (19)$$

in turn, for the galaxy (mass weighted):

$$[\mathrm{Z/H}] = -0.14(\pm0.02)\log(a) + 0.41(\pm0.04) \quad (20)$$

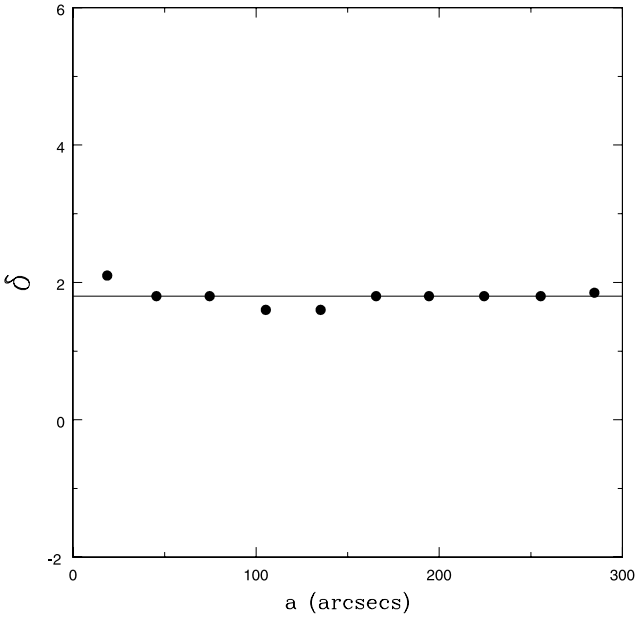

Figure 4. Behaviour of the δ parameter along the NGC 4486 semimajor axis (within 30 arcsec wide elliptical annuli). The horizontal line corresponds to $\delta = 1.80$.

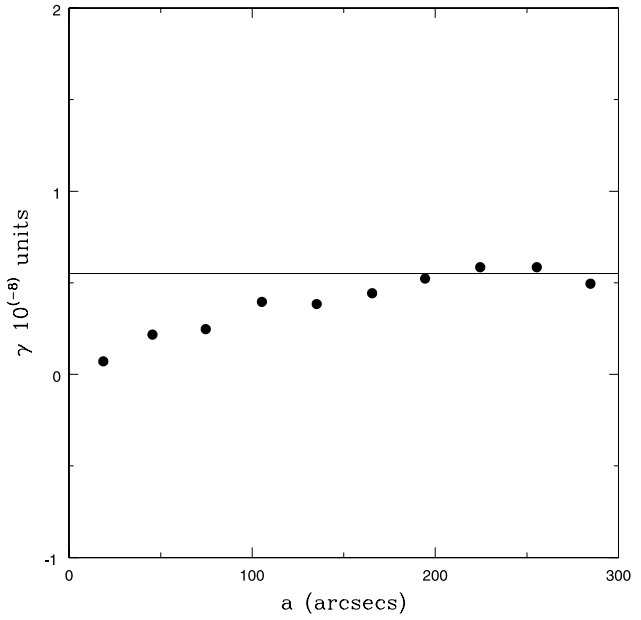

Figure 5. Behaviour of the γ parameter along the NGC 4486 semimajor axis (within 30 arcsec wide annuli). The sample includes only globulars brighter than the GCs turn-over magnitude, i.e. about 50 per cent of the total GC population. The decrease of this parameter towards the galaxy centre indicates a smaller number of GCs per unit of diffuse stellar mass. The horizontal line corresponds to $\gamma = 0.55 \times 10^{-8}$.

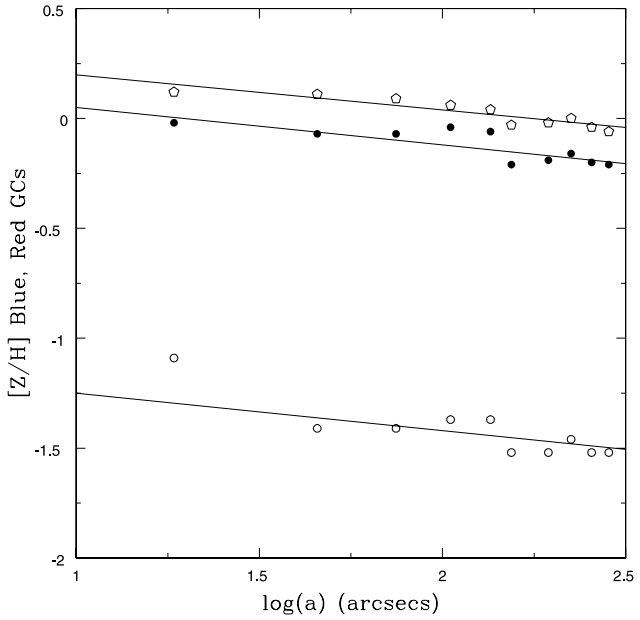

Figure 6. Chemical abundance [*Z*/H] gradient for the red (filled circles) and blue GCs (open circles), respectively (number weighted). Open pentagons represent the blue luminosity weighted abundance of the galaxy. The straight lines have a slope $\Delta[Z/H]/\Delta\log(a) = -0.17$.

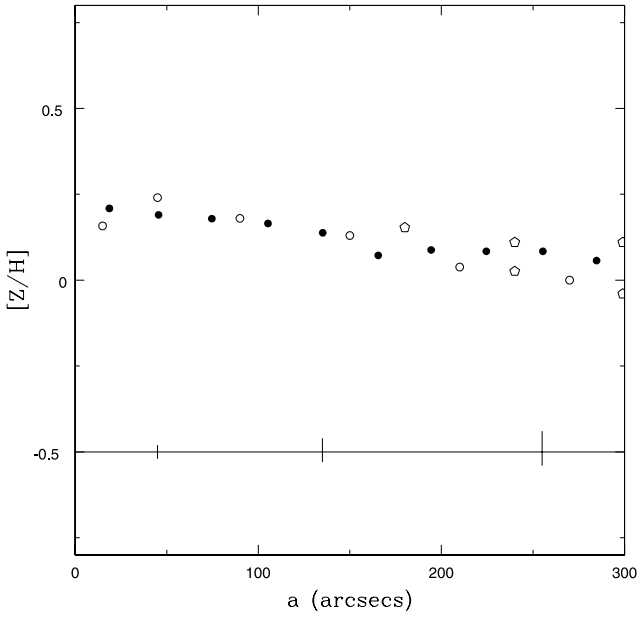

Figure 7. Chemical abundance [*Z*/H] inferred for the NGC 4486 stellar halo along its semimajor axis (solid dots). Open dots and pentagons are Fe abundances from X-ray observations given in Gastaldello & Molendi (2002) and Simionescu et al. (2010), respectively. The Fe abundances from these two works have been shifted upwards by 0.18. The vertical lines at the bottom show the effect of increasing/decreasing the adopted age by ±1.5 Gyr, then decreasing/increasing the inferred abundances (see text).

and (blue luminosity weighted):

$$[Z/H] = -0.16(\pm0.03)\log(a) + 0.36(\pm0.05). \quad (21)$$

The gradient fits corresponding to the GCs and to the galaxy (*B* luminosity weighted) are depicted in Fig. 6.

Excluding the [*Z*/H] value of the innermost blue clusters, the gradients of both GC sub-populations seem rather similar. However, taking into account the uncertainties of the derived coefficients, we cannot dismiss a lower or even null colour gradient for the blue GCs.

To within the uncertainties, our result is in very good agreement with Harris (2009) who finds galactocentric slopes of $-0.12(\pm0.02)$ and $-0.17(\pm0.03)$ for the blue and red GCs, respectively.

The significance of the [*Z*/H] value corresponding to the blue GCs in the innermost annulus would deserve further analysis since, if confirmed by other means (e.g. spectroscopy), it would imply an enhanced chemical enrichment process, probably at the very early stages of the formation of the galaxy.

Fig. 6 also shows another particular feature: the abundance residuals from the linear fits seem to occur in phase for both the blue and red GCs along the semimajor axis of the galaxy. A possible explanation to this effect would be differential interstellar reddening affecting the colours from which metallicities are derived. Such a kind of GC colour fluctuations is in fact seen in Fig. 3 (but not on the galaxy colours, as they come from a linear fit to the data in Michard's work).

In turn, Fig. 7 shows the (mass weighted) mean chemical abundance of the stellar population along the semimajor axis of the galaxy, as well as the Fe abundances determined by Gastaldello & Molendi (2002) and Simionescu et al. (2010) on the basis of hot gas X-ray observations (both set of observations were shifted upwards by 0.18 in ordinates). Stars and hot gas behave in a remarkably similar fashion suggesting a strong coupling.

The effects of changing the adopted age (12 Gyr) of the system on the chemical abundances, and following the prescription described in Section 2, are also shown in Fig. 7. As an example, the vertical bars correspond to an increase/decrease of 1.5 Gyr, leading to abundances that decrease/increase within a range of -0.05 to $+0.10$ in [*Z*/H]. The assumption of an older age would not have an impact on the overall gradient while a younger age would lead to an even shallower gradient.

The stellar mass spectrum inferred from equation (16), corresponding to $\delta = 1.80$, and convolved with a Gaussian kernel ($\sigma = 0.1$), are shown in Fig. 8 for two different ranges along the semimajor axis: within one effective radius (≈100 arcsec or 8 kpc; Caon et al. 1990) and within one to three times that value.

These distributions show a broad high abundance component with a peak that shifts towards smaller values with increasing galactocentric radius while the presence of a low-metallicity tail, reaching $[Z/H] \approx -2.0$, becomes more prominent.

Our inferred stellar mass–chemical abundance distribution has a strong similarity with the MDFs of resolved stars in NGC 5128 (Rejkuba et al. 2005; Rejkuba et al. 2011). From their analysis, these authors conclude that the bulk of the stars in NGC 5128 are 11 to 12 Gyr old and exhibit a range in chemical abundance that spans from $(Z/Z_{\odot}) \approx 0.007$ to 2.8.

The comparison, however, assumes that our stellar mass statistics are reflected as a number statistic (resolved stars), a valid reasoning only if the stellar mass function does not depend strongly on metallicity.

The detection of stellar haloes with low metallicity in resolved galaxies has been reported, for example, in NGC 3379 (Harris et al. 2007) and in NGC 4486 itself. In this galaxy Bird et al. (2010) find a low-metallicity tail, using *Hubble Space Telescope* observations. However, the limiting magnitude in this last work prevents a reliable assessment of the upper end of the metallicity distribution.

The presence of an extended stellar halo with low metallicity in NGC 4486 is also coherent with the detection of stars with ages

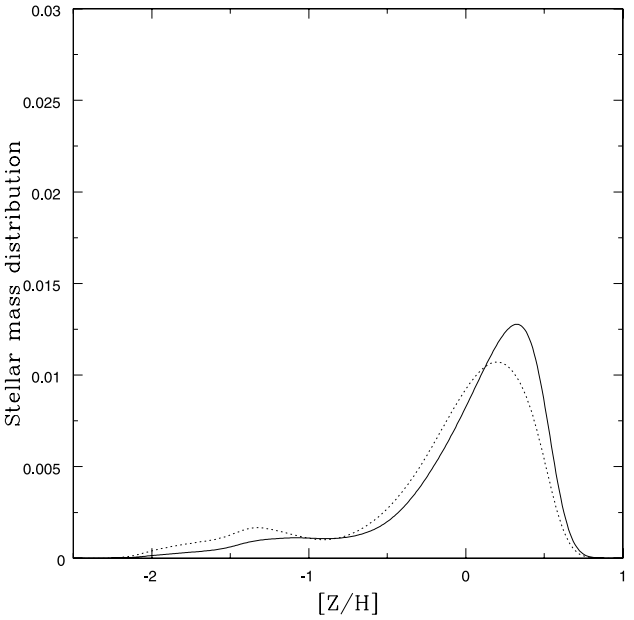

Figure 8. Inferred stellar MDF (normalized by total mass in units of relative mass per 0.01 dex in metallicity) for stars within two different ranges along the NGC 4486 semimajor axis: 100 arcsec (≈ one effective radius), solid line; and 100 to 300 arcsec. These distributions show the effect of the chemical gradient and the presence of a low-metallicity tail that becomes more evident in the outer region.

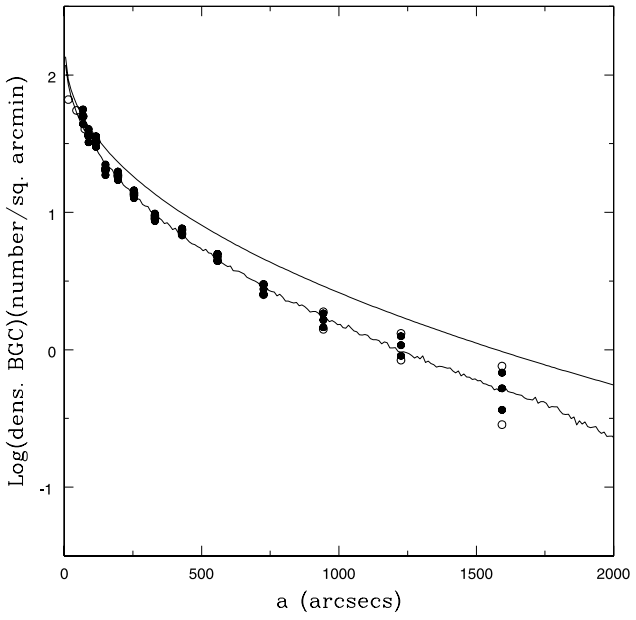

Figure 9. Blue GC areal density as a function of galactocentric radius (filled dots) from Harris (2009), showing the statistical uncertainties of the GC counts. The effect of a variation of 50 per cent on the adopted background is represented by open dots. The upper solid line corresponds to a Sérsic profile along the semimajor axis with constant ellipticity ($\epsilon = 0.40$) and characterized by $n = 2.20$ and $r_s = 43.0$ arcsec. The lower wavy line is the same model but sampled within circular annuli (i.e. within constant galactocentric distances).

older than 10 Gyr and metallicities below [Fe/H] ≈ -1.0, at large distances from the dominant Virgo galaxies (Williams et al. 2007).

5 LARGE-SCALE FEATURES: UP TO 1000 ARCSEC (80.4 KPC) ALONG THE GALAXY SEMIMAJOR AXIS

An extension of the previous discussion to a larger angular scale can be performed by combining the GC areal densities from Harris (2009) and the $(B - V)$ colour gradient of the galaxy presented by Rudick et al. (2010).

We start modelling the spatial distribution of the GC subpopulations, and then look for the δ and γ that provide the best fit both to the large-scale colour gradient and of the galaxy profile brightness. Those parameters, in turn, will allow the determination of the chemical abundance distribution and mass-to-luminosity (*M/L*) ratios for field stars, as well as of the total stellar mass.

5.1 Areal densities

A usual approach in the literature is the adoption of $r^{1/4}$ or of power laws in order to fit the GC areal densities as a function, for example, of galactocentric radius. Both Tamura et al. (2006) and Harris (2009) present this kind of analysis. Alternatively, the combination of their data with those given by Jordán et al. (2009) and FFG07, and taking into account the slightly different magnitude limits in these works, shows that Sérsic (1968) profiles can provide adequate fits even including the central regions of the galaxy, where GCs display core-like density profiles.

As a first step, we found the Sérsic parameters (scalelength r_s and n index) that fit the density profiles along the galactocentric radius (i.e. within circular annuli) for both GC populations. However, as already noted by McLaughlin, Harris & Hanes (1994), the GC system rather follows the galaxy flattening.

Taking this feature into account, we generated a model areal distribution which, in the case of the red GCs, follows the ellipticity of the galaxy halo ($\epsilon = 0.03$ at $a = 5$ arcsec to $\epsilon = 0.35$ at $a = 500$ arcsec). For the blue GCs we set a constant ellipticity ($\epsilon = 0.40$). This last procedure seems justified since, in the outer regions, both the galaxy and the blue GC population exhibit a similar ellipticity (see fig. 4. in Tamura et al. 2006). Comparable values of the ellipticities of the red and blue GC distributions have been presented in the extensive work by Strader et al. (2011).

The galactocentric (wavy lines) and semimajor axis (continuous line) density runs of the models are shown in Fig. 9 for the blue GCs ($r_s = 43$ arcsec, $n = 2.20$, central density = 170 clusters per square arcmin) and in Fig. 10 for the red GCs ($r_s = 13.5$ arcsec, $n = 2.35$, central density = 350 clusters per square arcmin). These diagrams also display the uncertainties of the profiles as a result of the adopted background and GC counting statistics.

5.2 $(B - R)$ colours

In order to fit the integrated colours of the galaxy we followed the approach described in Section 3, adopting the GC areal density profile models to determine the number of blue and red GCs along the semimajor axis (previous subsection).

In turn, the variation of the GC chemical abundance scales within 300 arcsec were approximated through linear relations:

$$\log(Z_{SB}) = -0.25(\pm 0.02)\log(a) - 1.02(\pm 0.07) \quad (22)$$

for the blue GCs, and

$$\log(Z_{SR}) = -0.25(\pm 0.03)\log(a) + 0.55(\pm 0.07) \quad (23)$$

for the red GCs, which are compatible with the abundance gradient derived from Table 1 (since $\Delta[Z/H]/\Delta\log(Z_s) = 0.69$ for both GC

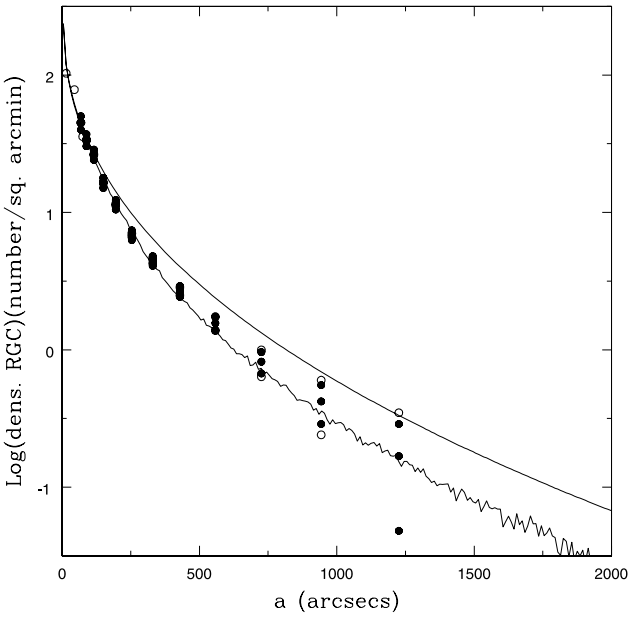

Figure 10. Red GC areal density as a function of galactocentric radius (filled dots) from Harris (2009), showing the statistical uncertainties of the GC counts. The effect of a variation of 50 per cent on the adopted background is represented by open dots. The upper solid line corresponds to a Sérsic profile along the galaxy semimajor axis, following the galaxy ellipticity variation, and characterized by $n = 2.35$ and $r_s = 13.5$ arcsec. The lower wavy line is the same model but sampled within circular annuli (i.e. within constant galactocentric distances).

sub-populations). As a first approach these gradients were extrapolated outwards $a = 300$ arcsec.

The $(B - R)$ colour gradients are displayed in Fig. 11, where large open dots represent the best-fitting model corresponding to $\delta = 1.70$, while the straight line is the (transformed) Rudick et al. (2010) colour gradient.

The δ parameter, in this case, is about 6 per cent smaller than that derived in Section 4. The difference arises because the colour gradient from Rudick et al., $\Delta(B - R)/\Delta\log(a) = -0.14$, is slightly steeper than that derived from the Michard (2000) data for the innermost regions.

Fig. 11 also includes the colour gradients of the halo and bulge stars, both governed by the metallicity gradients discussed in Section 4. Although these gradients are rather similar, the shape of the colour–metallicity relation leads to a shallower colour slope for the halo, a behaviour shared by the blue GCs, and also found in other galaxies (e.g. Forbes et al. 2011; Faifer et al. 2011).

As an important result, Fig. 11 indicates that most of the colour gradient of the galaxy arises from the luminosity weighted composition of the halo and the bulge, whose relative contributions change along the semimajor axis. The metallicity gradients of each sub-population seem to play a relatively minor role regarding the composite stellar colour gradient. For example, adopting null colour gradients outwards $a = 300$ arcsec yields $(B - R)$ colours that are only 0.015 mag redder at $a = 1000$ arcsec.

Finally, as seen in Fig. 11, the model integrated colours keep within ± 0.01 mag from the observed ones and do not seem to require a significant variation of the stellar age, as reported in the photometric study by Liu et al. (2005).

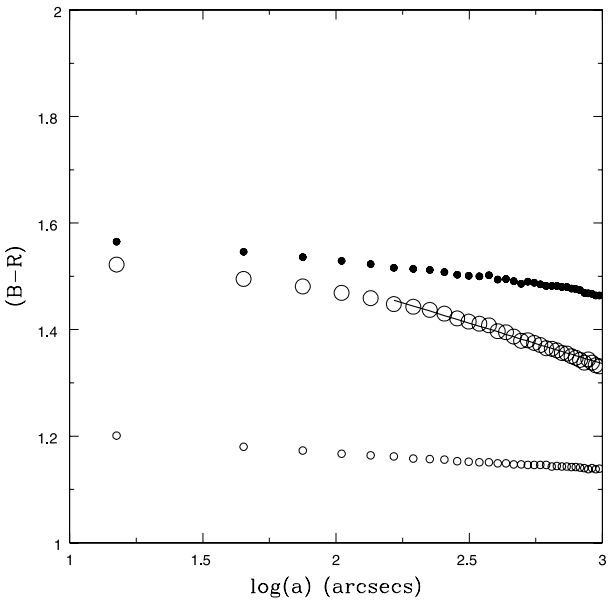

Figure 11. Logarithmic $(B - R)$ colour versus semimajor axis a. Large open dots (0.01 mag in radius) are the model colours obtained for the galaxy and adopting $\delta = 1.70$. The straight line is the colour gradient derived from Rudick et al. (2010) transformed to $(B - R)$. Filled dots represent the bulge colours while open small circles correspond to the halo colours, both inferred from the abundance gradients, discussed in Section 5.2.

5.3 The NGC 4486 brightness profile

The Caon et al. (1990) B profile adopted in this work, and shown in Fig. 12, is in good agreement with previous ones (e.g. the EW profile by de Vaucouleurs & Nieto 1978, or the photographic work

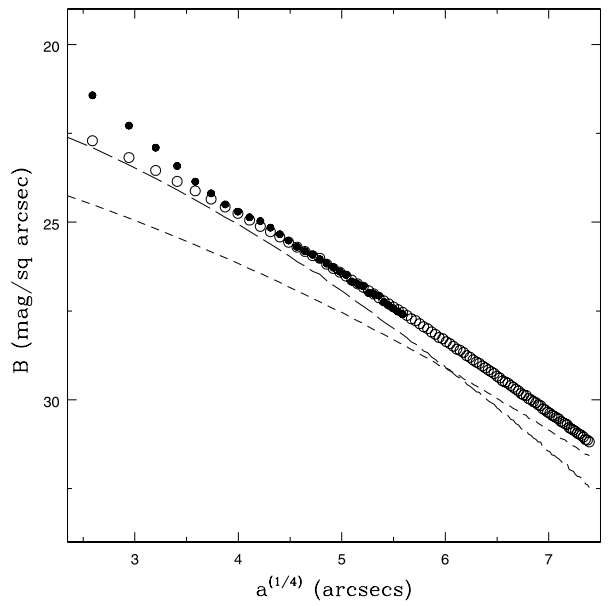

Figure 12. NGC 4486 B surface brightness profile from Caon et al. (1990), (dots) compared with the model profile derived using the GCs as stellar population tracers (open dots). The short and long dash lines correspond to the brightness contributions arising in the halo and bulge, respectively, as traced by the blue and red GCs. The profiles are extrapolated between $a^{1/4} = 5.62$ ($a = 1000$ arcsec) and $a^{1/4} = 6.69$ ($a = 2000$ arcsec).

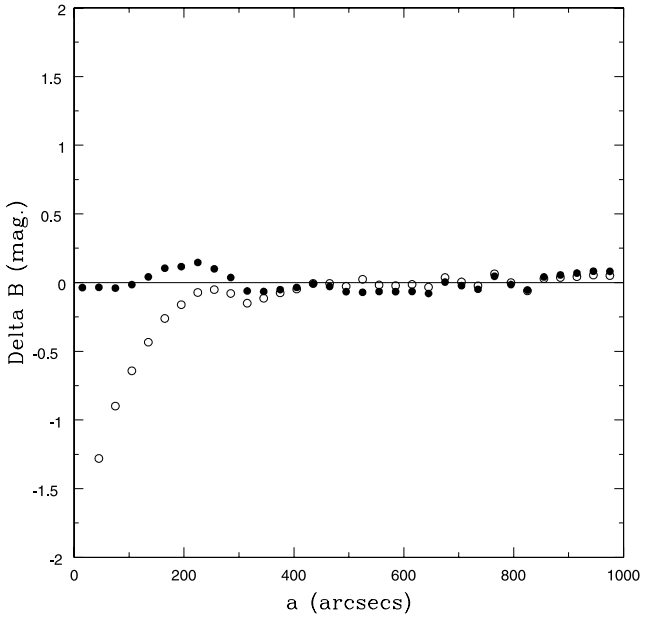

Figure 13. Brightness profile fit residuals using the GCs as luminosity tracers (open dots), compared with those arising from a single Sérsic profile characterized by $n = 10.0$. The strong deviation within ≈250 arcsec is attributed to GC erosion by dynamical effects (see text).

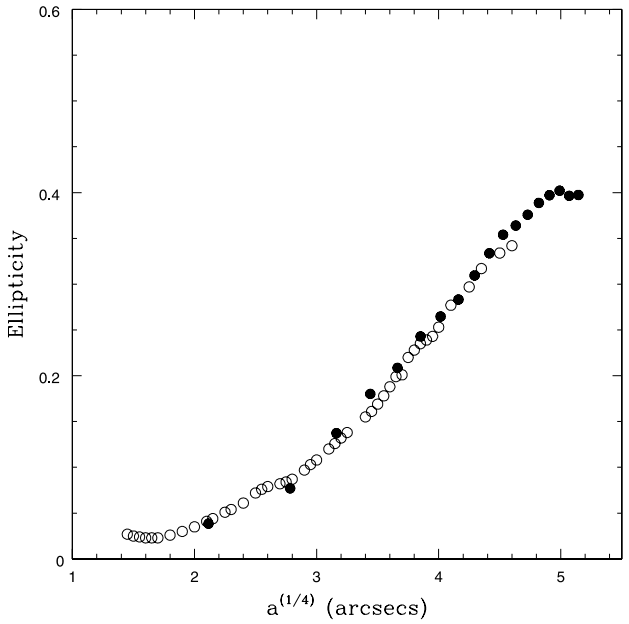

Figure 14. Ellipticity variation along the semimajor axis of NGC 4486. Open dots are observed values from Caon et al. (1990). Filled dots correspond to the bi-dimensional surface brightness model described in the text.

by Carter & Dixon 1978), as can be seen in the comparison presented by Liu et al. (2005).

A single Sérsic profile fit gives $n = 10 \pm 2$ for a galactocentric range that covers from $a = 20$ arcsec to $a = 1000$ arcsec. The residuals, displayed in Fig. 13, correspond to an overall rms $= \pm 0.07$ mag. The innermost region of the galaxy was not included to avoid the complex structure connected with the NGC 4486 jet as well as seeing effects. A similar fit, transforming the Caon et al. (1990) B photometry to the V band, through the Rudick et al. (2010) $(B - V)$ colours, leads to $n(V) = 9.5 \pm 2$.

Alternatively, we used GCs as 'brightness tracers'. In this case, each 'diffuse' stellar mass element (equation 16) was spatially distributed following the description given in Section 5.1 and, after adopting $\gamma = 0.55 \times 10^{-8}$ and $\delta = 1.70$, transformed to B luminosity to generate a bi-dimensional image of the galaxy. This image was analysed with the IRAF package to obtain the model surface brightness profile. The variation of the model ellipticity along the semimajor axis of the galaxy is compared with the observed one in Fig. 14.

The brightness residuals obtained by comparing the observed and model profiles, also depicted in Fig. 13, are very similar to those arising from the Sérsic profile outwards $a = 250$ arcsec.

The systematic trend of these residuals towards the centre of the galaxy is consistent with the behaviour of the γ parameter shown in Fig. 5, and with the possible destruction of GCs by dynamical effects. Reconciling the observed brightness profile with that traced by the GCs implies that we currently observe 85 and 60 per cent of the original blue and red GC populations, respectively.

We stress that the completeness factors of the photometric works by FFG07 and Jordán et al. (2009) are higher than 90 per cent for GC candidates brighter than the turn over of the GC luminosity function, then ruling out that this trend could be eventually caused by instrumental or galaxy background effects.

Our two components (halo and bulge) fit has some similarities with the approach presented by Seigar, Graham & Jerjen (2007) who found that the brightness profiles of five cD galaxies are better represented by combining two Sérsic profiles with different n indices and scalelengths. In particular, they noticed the common presence of outer exponential haloes ($n = 1.0$). This result, in a first approximation, is not in conflict with ours since forcing $n = 1.0$ leaves brightness residuals smaller than ± 0.05 mag for the halo component, within a range of $a = 250$ arcsec to $a = 1000$ arcsec.

Fig. 12 also suggests that the brightness of the extended halo should equal the bulge brightness at $a \approx 1300$ arcsec (104 kpc) and that, presumably, would become dominant outwards. This result is consistent, but better constrained than that in FFG07, mainly due to a more reliable definition of the colour gradient of the galaxy on an extended angular scale.

5.4 A comparison between the chemical abundance of globular clusters and field stars

The chemical abundance distribution function for the blue GCs and halo stars, as well as for the red GCs and bulge stars, within $a = 1000$ arcsec (80.4 kpc), is depicted in Figs 15 and 16. These diagrams show mean stellar abundances about 1.6 times (0.2 dex) larger than those of the GCs.

Preliminary interpretations of these mass-chemical abundance spectra can be made along the usual pathways, i.e. assuming that Z is a 'clock' as in simple models or, alternatively, that chemical abundance is rather a volume 'sampler' as in the inhomogeneous enrichment models.

A search of the literature shows that the inferred MDF of the bulge stars is rather similar to the 'push' model put forward by Schombert & Rakos (2009). These authors artificially modify the output of an infall model by reducing the low-metallicity end of the stellar population in an attempt to assess the impact on the integrated model colours of elliptical galaxies and to avoid the *'infamous G-dwarf problem'*.

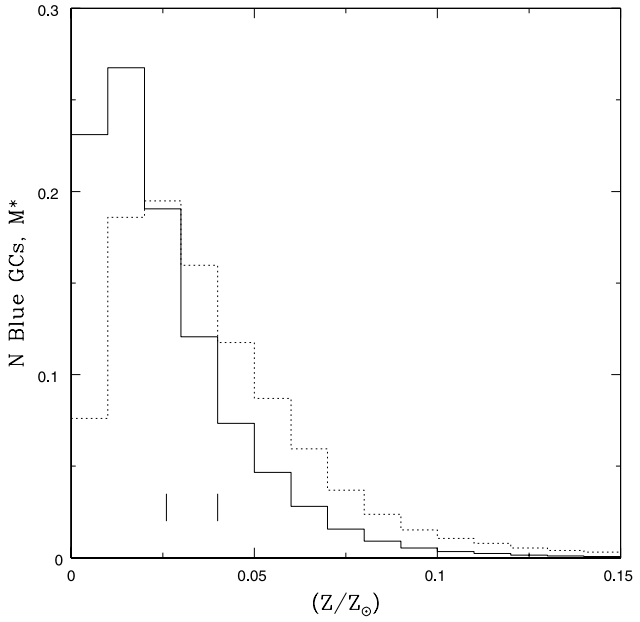

Figure 15. Chemical abundance distribution (in solar units) for the blue GCs within $a = 1000$ arcsec (80.4 kpc) normalized by total number (solid histogram) and for the halo stars, normalized by total mass (dotted histogram). Vertical lines at $(Z/Z_\odot) = 0.026$ and $(Z/Z_\odot) = 0.040$ indicate the mean chemical abundance for clusters and stars, respectively.

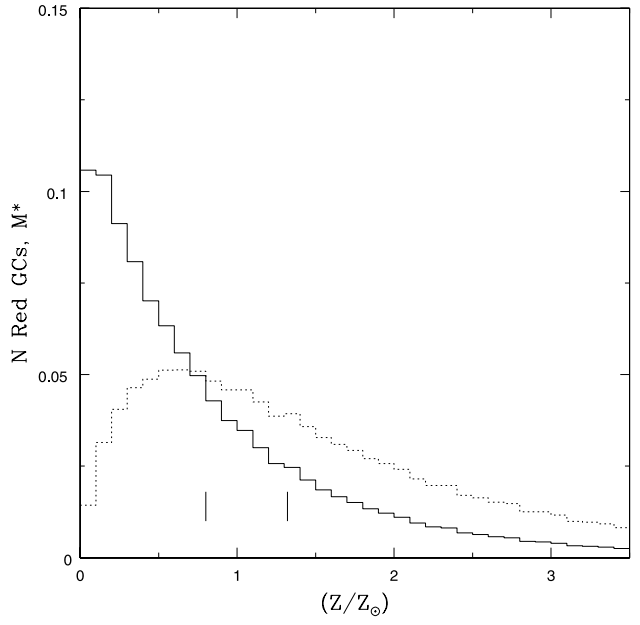

Figure 16. Chemical abundance distribution (in solar units) for red GCs within $a = 1000$ arcsec (80.4 kpc), normalized by total number (solid histogram) and for the bulge stars, normalized by total mass (dotted histogram). Vertical lines at $(Z/Z_\odot) = 0.80$ and $(Z/Z_\odot) = 1.32$ indicate the mean chemical abundance for clusters and stars, respectively.

They also reject the simplest chemical evolution scenarios and, at the same time, point out the similarity of their tentative approach with the results from inhomogeneous enrichment models (Oey 2000) which also provide a better representation of the high-metallicity drop-off of the MDFs.

The abundance distributions in the inhomogeneous enrichment models are the result of star formation in different events that eventually overlap, and are characterized by the product nQ, where n is the number of stellar generations and Q is a filling factor that measures the relative volumes of enriched and primordial gas.

In particular, we note the similarity of the MDFs presented in this work and those depicted in Oey's figs 2 and 3, corresponding to the halo and bulge of the MW, which require low and high nQ values, respectively. It is tempting to connect these results with the fact that the γ and δ parameters derived in previous sections imply that ≈50 per cent of the blue GCs form associated with diffuse stellar masses below $10^7\,M_\odot$, and with masses below $12 \times 10^7\,M_\odot$ in the case of the red GCs.

Another intriguing result is suggested by Oey's fig. 1 (panel c). That diagram shows the decoupling of the MDFs characterizing the very early stellar generations from the composite one at the end of the whole star-forming process. In this scenario, the first stellar generations still reflect the so-called 'metal production function' $f(Z)$, which is assumed to be a power law (decreasing with Z) governed by SNe enrichment. In our analysis, GCs follow a comparable trend (although with an exponential dependence) and could be in fact mapping such $f(Z)$ if their formation is restricted to the initial stellar generations.

In either case, the landscape seems coherent with Spitler (2010), who argues in favour of an intense formation of bulge GCs followed by an era of stellar bulge growth and little cluster production.

5.5 Stellar mass-to-luminosity ratio

The dependence of the mass to B luminosity ratio with chemical abundance adopted in this work (equation 17) was used to determine integrated ratios for galaxies in the Virgo cluster (FFV09). The ratios inferred in that work are in perfect agreement with those reported by Napolitano, Romanowsy & Tortora (2010) through a completely different approach.

Using the same dependence, the chemical gradients described before, and adopting $\delta = 1.70$ (Section 5.2), we derived the mass-to-luminosity ratios for the B and V bands (within elliptical annuli 30 arcsec wide in a) for the composite stellar population, i.e. including both halo and bulge stars, that are plotted in Fig. 17 and correspond to an overall integrated ratio $(M/L)_B = 8.3$.

Most of the variation of the (M/L) ratios in this last figure, as in the case of the colour gradient of the galaxy, is governed by the change of the mass ratio of halo to bulge stars with galactocentric radius. Halo stars alone, in fact, show a rather limited range of the $(M/L)_B$ ratio, which falls from 4.4 to 4.2 within the inner 120 arcsec and levels off at ≈4.0, outwards.

Recently, Gebhardt & Thomas (2009) and Murphy, Gebhardt & Adams (2011) made an extensive analysis of the stellar and GC kinematics in NGC 4486. Their dynamical model includes a super massive black hole, stars and dark matter. The (M/L_V) ratio shown in Fig. 17 is comparable to $(M/L)_V = 6.3 \pm 0.8$, given in the first paper, but significantly lower than the range $(M/L)_V = 8.2$ to 9.1 reported in the second work.

6 STELLAR AND DARK MATTER MASSES

The halo, bulge and total (projected) cumulative masses are shown in Fig. 18. These curves were obtained by combining the Caon et al. photometry and the $(M/L)_B$ ratios discussed in the previous section within $a = 1000$ arcsec. Outwards, where the stellar mass contributes with only ≈10 per cent of the total, we assumed constant ratios set by the outermost $(M/L)_B$ value.

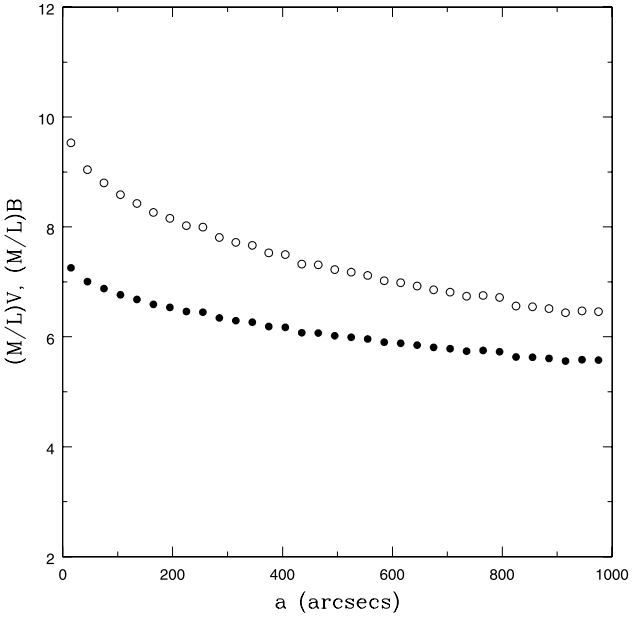

Figure 17. Inferred blue (open dots) and visual (filled dots) mass-to-luminosity ratios within 1000 arcsec (80.4 kpc) along the NGC 4486 semimajor axis and within 30 arcsec annuli following the variation of the ellipticity of the galaxy.

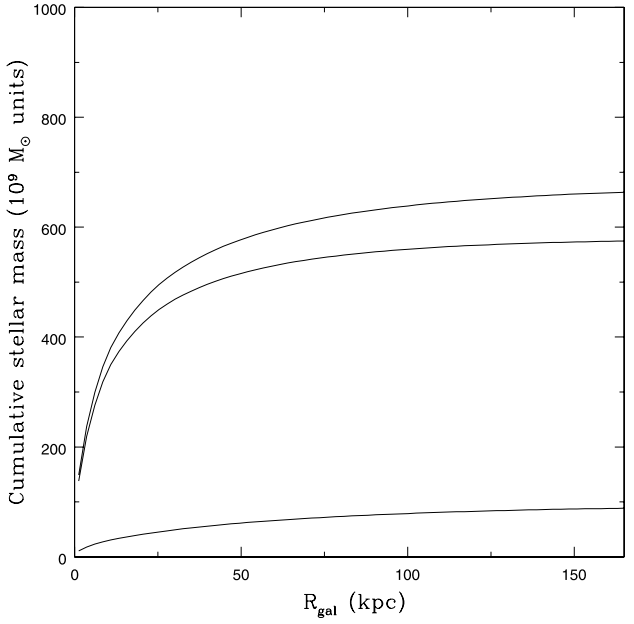

Figure 18. Cumulative stellar mass as a function of galactocentric radius for the total (upper curve), bulge (middle curve) and halo (lower curve) stellar populations. The half (projected) mass radii for the bulge and the halo are 8.4 kpc (105 arcsec) and 28 kpc (350 arcsec), respectively.

Using kinematic data of planetary nebula, Doherty et al. (2009) determine the 'edge' of the NGC 4486 halo to be at ≈2000 arcsec (164.8 kpc), which is the adopted upper galactocentric limit in Fig. 18. Within this galactocentric radius we obtain a total stellar mass of $6.8(\pm1.1) \times 10^{11}\,M_{\odot}$. This mass is consistent the Sérsic index n_V versus stellar mass relation derived by D'Onofrio et al. (2011) (see their fig. 1, upper-left panel) in an analysis of the connection between the shape of early-type galaxies and their stellar populations.

Our estimate of the mass uncertainty, about ±15 per cent, comes from errors of ±0.05, and ±0.10, for the γ and δ parameters, respectively, and of ±0.25 mag for the integrated blue magnitude of the galaxy ($B = 9.50$).

Fig. 18 indicates that the halo and the bulge make different contributions to the total stellar mass (14 and 86 per cent, respectively) and also that these subsystems have very distinct spatial distributions characterized by half-mass projected radii of 110 and 350 arcsec (8 and 28 kpc, respectively).

A similitude between the projected blue GCs areal density given by FFG07 and that of dark matter in NGC 1399 (from Richtler et al. 2004) was pointed out in Forte, Faifer & Geisler (2005), and still holds after the recent and improved analysis by Schuberth et al. (2010) (see their models a10 and b10). The same comparison can be performed for NGC 4486 using the results presented by Gebhardt & Thomas (2009) and Murphy et al. (2011).

In this case, and even though the total enclosed mass derived by those authors are in good agreement (2 to $3 \times 10^{13}\,M_{\odot}$ within 160.8 kpc), their inferred spatial distributions for dark matter are significantly different. Under the assumption of a logarithmic potential to represent the dark halo, those works obtain core radii in the range from 164 to 414 arcsec.

The corresponding dark matter volumetric density profiles (equation 3 in Gebhardt & Thomas 2009), once projected on the sky and given on a pseudo-magnitude scale arbitrarily shifted in ordinates, are displayed in Fig. 19. As the outer spatial limit of the dark matter halo is not well constrained we adopted two tentative values in order to assess the impact on the projected profile. The lower curves correspond to a cut-off radius of 2500 arcsec, i.e. 25 per cent larger than that given by Doherty et al. (2009), while the upper curve corresponds to twice that radius.

This figure also shows the inferred surface brightness profile of the stellar population with a chemical abundance lower than

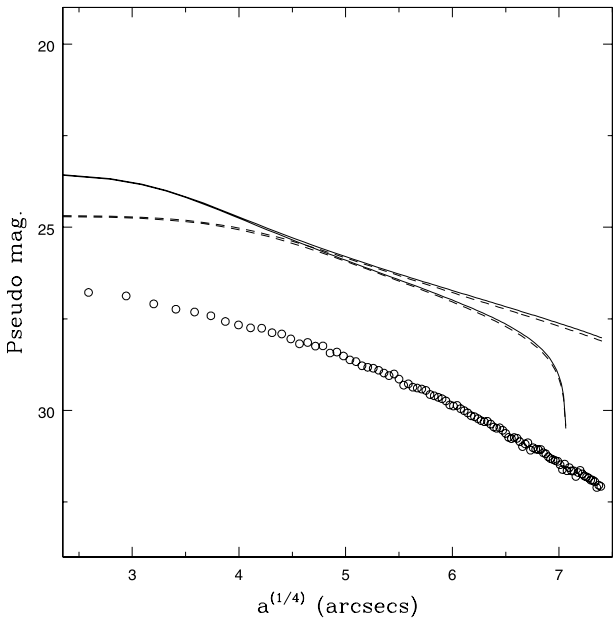

Figure 19. A comparison between the projected dark matter density profiles (on a pseudo-magnitude scale) from Gebhardt & Thomas (2009) (continuous line) or Murphy et al. (2011) (dashed line), with the inferred surface brightness of stars with $(Z/Z_{\odot})$ less than 0.025 (open dots), along the NGC 4486 semimajor axis. The projected dark matter profiles correspond to cut-off radii of 2500 arcsec (lower curves) and 5000 arcsec (upper curves), respectively.

$(Z/Z_{\odot}) = 0.025$. These stars are connected with GCs bluer than the 'blue peak' [at $\approx(C - T_1) = 1.25$] of the cluster colour distributions.

A meaningful comparison closer to the centre of the galaxy (i.e. within 250 arcsec) becomes blurred by dynamical erosion on the blue GCs, used as tracers of the stellar component, and would require a rigorous assessment of these effects.

Even though dark matter and very low metallicity stars display rather similar projected distributions, a comparison between their spatial distributions still remains somewhat ambiguous due to the uncertain cut-off radius of the halo. On the one hand, adopting the Doherty et al. (2009) value would suggest that these stars in fact 'map' the dark halo. Alternatively, doubling that cut-off radius leads to a somewhat shallower distribution for dark matter. In fact, Strader et al. (2011) do not find evidence for a transition in the inner halo to a potential dominated by the Virgo cluster.

A shallower distribution of the dark matter is predicted by the Abadi, Navarro & Steinmetz (2006) models for isolated galaxies, where an extended halo develops by accretion of stars shed from early merging sub-units, in a hierarchical galaxy formation scenario. A further and rigorous comparison, however, should take into account the distinct environmental situation of NGC 4486 as a central galaxy in the Virgo cluster.

The results discussed in this section also allow an estimate of the baryon fraction ($f_{\rm b}$) in NGC 4486, which we restrict to a galactocentric radius of 80.4 kpc aiming at avoiding the inherent uncertainties that become more important at larger radii. The total baryonic mass within that boundary is $8.8 \times 10^{11}\,{\rm M}_{\odot}$, from which $6.8 \times 10^{8}\,{\rm M}_{\odot}$ corresponds to stars and $2.0 \times 10^{11}\,{\rm M}_{\odot}$ to hot gas. This last mass was derived from Fabricant & Gorenstein (1983) after correcting the distance to NGC 4486 to the value adopted in this work (15 Mpc). On the other side, the total enclosed mass in both Gebhardt & Thomas (2009) and Murphy et al. (2011) is close to $10^{13}\,{\rm M}_{\odot}$, then yielding a fraction $f_{\rm b} = 0.08$. This value is well below the cosmic baryon fraction (0.17). However, combined with the circular velocities (715 to 800 km s^{-1}) given in these last two works, it falls close, and within the dispersion, of the baryonic fraction-versus-circular relation presented by Dai et al. (2010) (see their fig. 4).

7 GLOBULAR CLUSTER FORMATION EFFICIENCY

The estimated number of blue and red globulars within $a =$ 2000 arcsec, assuming a fully Gaussian GC integrated luminosity function (12 200 $\pm$ 1500 and 4600 $\pm$ 1000), corresponds to a specific S_n frequency close to 14 $\pm$ 1.5 and is consistent with the already known nature of NGC 4486 as an archetype 'high S_n system'.

The number of GCs, and the halo and bulge masses discussed in Section 6, yields the intrinsic GCs formation efficiency for each subsystem in terms of the associated halo mass $\log(t_B) = 2.15$, or bulge mass, $\log(t_R) = 0.90$ (both given in 10^{-9} units). These values are shown in Fig. 20 and compared with the locus corresponding to GCS in Virgo galaxies, derived from a re-discussion of the FVF09 data. In this last work, we note the definition of GC formation efficiency is that given by Zepf & Ashman (1993), i.e. in terms of the total stellar mass of the galaxy (see also Rhode, Zepf & Santos 2005).

Fig. 20 also shows the MW GC formation efficiencies, after adopting the halo and bulge masses from the discussion presented by Boley et al. (2009), and a number of 110 halo and 35 bulge GCs (Mackey & van den Bergh 2005; Bica et al. 2006). The MW clusters also show a much higher formation efficiency for the halo GCs, and

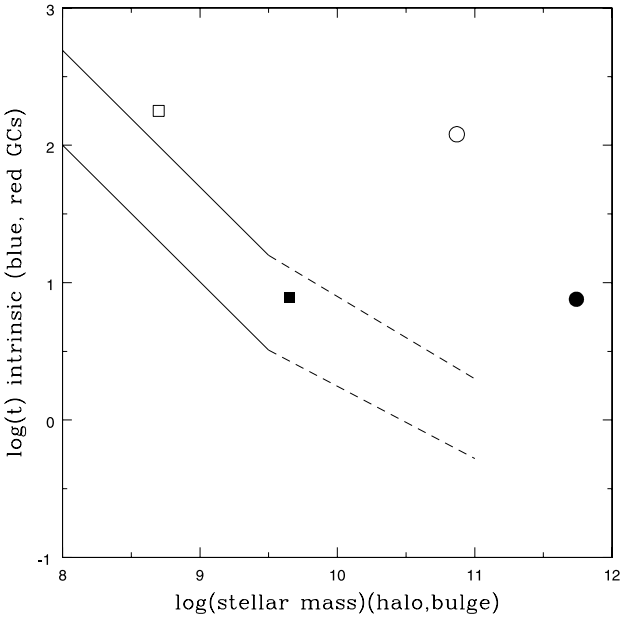

Figure 20. GC intrinsic formation efficiency locus for the blue (solid lines) and red (dash lines) sub-populations associated with 63 galaxies in the Virgo cluster. The open and solid dots represent the integrated values of the blue and red GCs associated with NGC 4486, respectively. Squares correspond to the MW GCS.

compare well with the Virgo GCS locus which, in principle, seems dominated by galaxies that have suffered minor merging events. Even though the GC formation efficiencies presented in this work depend on the assumed connection between the number of GCs and the diffuse stellar mass (Section 3), those of the MW GCs come from a completely independent approach.

The reason behind the strong difference in the formation efficiency of halo and bulge globulars is not clear. However, a distinctive feature between both systems, besides metallicity, seems to be the mean density of the associated stellar populations. A first estimate of these densities, using the half-mass radii and stellar masses given in the previous subsection, indicates a mean bulge stellar density an order of magnitude higher than in the halo. This suggests that the erosion of potential GC formation sites by field stars may be more important in the bulge environment then leading to a lower cluster formation efficiency.

In turn, Fig. 20 indicates that dry merging might have provided both the halo stellar mass and the high number of blue GCs in NGC 4486 through some 300 galaxies with indicative masses of $\approx 30 \times 10^{7}\,{\rm M}_{\odot}$.

Within this frame, and as a tentative approach, we created a 'composite' galaxy using the Jordán et al. (2009) data corresponding to 10 Virgo galaxies with more than 50 blue GCs each.

As some works indicate that galaxies can reach masses $\approx 10^{10.8}\,{\rm M}_{\odot}$ before the star-forming process is self-interrupted (see Khochfar & Silk 2009), this limit was adopted to define the upper mass of the galaxies in the sample: VCC 685, 698, 759, 1062, 1231, 1279, 1297, 1327, 1692 and 2000. That value is close to $10^{11}\,{\rm M}_{\odot}$, upper mass of the galaxies that define the 3D plane discussed in FVF09.

The total population of the composite galaxy includes 916 GC candidates brighter than the NGC 4486 GCs turn-over magnitude ($g = 23.87$ mag; Villegas et al. 2010).

From the analysis of this data set we emphasize the following points.

(a) The composite GCs colour–magnitude diagram shows a blue tilt similar to the tilt observed for the blue GCs in NGC 4486.

(b) A fit similar to those given in Table 1 leads to GC chemical scalelengths of $Z_{\rm SB} = 0.015$ and $Z_{\rm SR} = 0.55$.

(c) The blue GCs chemical scale parameter, $Z_{\rm SB}$, is comparable to that expected for the blue GCs in the outer regions of NGC 4486.

(d) The red GC colours can be adequately fit by a single $Z_{\rm SR}$ parameter even though they are the result of composing galaxies that exhibit a large range in their individual parameters (0.12 to 0.90).

These results give support to the idea that the blue tilt is a generalized feature in most Virgo galaxies and could be detected even after eventual merging processes.

Although the accretion of low-mass galaxies might have provided an important fraction of the NGC 4486 halo mass, as suggested in the *naive* approach by Forte, Martinez & Muzzio (1982), the presence of a metallicity gradient for the blue GCs rather indicates that dissipative collapse has also played a role.

On the other hand, dry merging alone cannot explain the characteristics of the red GCs bulge in NGC 4486 since the inferred $Z_{\rm SR}$ parameters in this galaxy reach values that are twice as those of the individual galaxies with comparable t_R in Fig. 20. The result commented in item *d* is also interesting in the sense that eventual multiple mergers will not yield detectable effects on the (almost always) bimodal colour distributions.

8 CONCLUSIONS

The distribution of the integrated GC colours in NGC 4486 is compatible with the presence of two different (blue and red) populations both following an exponential decay (in number) with increasing chemical abundance *Z*. The chemical scalelengths, however, are very different, being much smaller for the blue GC family. Both GC chemical scales have negative gradients with increasing galactocentric radius. In turn, the composite mass weighted chemical gradient obtained for the composite stellar population is comparable to that derived through X-ray observations of hot gas, indicating a strong connection between stars and the interstellar medium.

The main idea behind the GCs–field stars connection adopted in this work is that the metallicity of a given cluster is a proxy to the mass of the associated diffuse stellar population where it is born and which, through pre-enrichment (see Bailin & Harris 2009), determines the cluster metallicity itself. Furthermore, metallicity may be indicative of the mean stellar density of the environment, a factor possibly governing the GCs formation efficiency.

The approach allows, by combining both the halo and bulge components, the reconstruction of the galaxy profile brightness and of the negative integrated colour gradient over an angular scale of, at least, 1000 arcsec (≈80 kpc). Given the multi-metallicity nature of the stellar population, Single Stellar Population (SSP) models are not adequate for a proper understanding of integrated colours in terms of chemical abundance (for a detailed discussion on this subject, see Schombert & Rakos 2009).

The chemical abundance distribution inferred in this work for the stellar population is similar to those observed in resolved galaxies and exhibits similarities with the predictions given by heterogeneous enrichment models as discussed by Oey (2000).

In particular, the halo/bulge systems can be identified as formed in low-/high-density environments typified by small/large number of stellar generations and different filling factors. A comparison of our Figs 15 and 16 with figs 2 and 3 in Oey's work appeals for a further, more quantitative exploration.

If GCs appear at the very beginning of the star-forming process their own chemical distribution may be reflecting the original 'metal production function' and this would also imply larger mean ages than that of the field stars. In agreement with this, Spitler (2010) suggests that metal-rich GCs should be older by about 1 Gyr compared with the average age of the bulge.

The GC formation efficiency for each (halo, bulge) system shows that the NGC 4486 system clearly deviates from those corresponding to other Virgo galaxies with masses smaller than $10^{11}\,{\rm M}_{\odot}$.

Although both the NGC 4486 stellar halo mass and the large number of blue globulars could be reached by accreting low-mass galaxies, the presence of a chemical abundance gradient rather suggests that accretion might have coexisted with the in situ formation of indigenous blue GCs (see Harris 2009 or Forbes et al. 2011 for a similar conclusion). A description of the mechanisms that may play a simultaneous role in the formation of galaxy haloes is given, for example, in the model analysis by Murante et al. (2007).

We also stress that the eventual accretion of an external population of blue clusters, through numerous small mergers, would not affect the detectability of the chemical or colour gradient of the indigenous blue GCs or of the blue tilt (as shown in Section 7). Alternatively, but not in necessary disagreement, Kissler-Patig & Gebhardt (1998) argue that their detection of rotation for the blue GCs is possibly the fingerprint of an important single past merger.

On the other hand, pure dry merging cannot explain the red GC–bulge population since the chemical scale parameter of the plausible progenitor galaxies is much smaller than that in the central region of NGC 4486. Both dissipative collapse and/or wet merging leading to high star-forming efficiencies and chemical enrichment seem required. The low central surface brightness, as well as the shallow chemical gradient in NGC 4486, is compatible with merging processes (e.g. Kim, Shin & Jin 2010). This is also suggested by the position of the galaxy in the Sérsic *n* index-versus-central brightness relation 'normal' ellipticals (see Graham & Guzmán 2003 for a comprehensive discussion). A scenario where GC formation is in fact entirely merger-driven is given in Muratov & Gnedin (2010).

The spatial distribution of the halo stars with the lowest chemical abundance is remarkably similar to that inferred for dark matter. This coincidences was already noticed in the case of NGC 1399 (Forte et al. 2005). This last galaxy and NGC 4486 seem to have a very similar baryonic mass (see Jones et al. 1997) and also a comparable number of red GCs. However, they differ both in the number of blue GCs and dark mass content by the same factor, which is ≈3 larger in NGC 4486. Besides, a re-discussion of the photometric data presented in FFG07 and of the dark matter content presented by Schuberth et al. (2010) for NGC 1399 also indicates a remarkably similar number of blue GCs per dark mass unit, $\approx 1.0(\pm 0.3) \times 10^{-9}$ in both galaxies.

All these features add to the discussion of the possible origins of GCs, and in particular of the blue clusters, in connection with primordial dark matter sub-haloes (e.g. Santos 2003; Mashchenko & Sills 2005; Bekki et al. 2008; Boley et al. 2009).

Further arguments about the connection between GCs and dark matter come from the very large scale study by Lee et al. (2010), who report the detection of 'intracluster' GCs whose projected spatial distribution resembles those of dwarf galaxies and dark matter on

very large angular scales. The change in the slope of the GC areal density profile in their work, at ≈40 arcmin (193 kpc) from the centre of NGC 4486, is close to the 'edge' of the galaxy halo as determined by Doherty et al. (2009) (but see Strader et al. 2011 for a different conclusion).

The analysis presented in this work strongly supports the idea that GCs appear along the main star-forming events in early-type galaxies and can be used as tracers of the dominant stellar populations. The 'two phases' process, as suggested by Forbes, Brodie & Grillmair (1997), seems an adequate scenario to explain the overall features of GCs and associated stars. The meaning of 'phase', however, may require further clarification in terms of the existence of a temporal sequence (i.e. halo globulars appear prior to bulge globulars as suggested by the very different chemical abundances), environmental differences (underlying in the inhomogeneous enrichment models) and, eventually, about how both factors combine in the overall landscape of galaxy formation.

ACKNOWLEDGMENTS

JCF acknowledges Dr. Stephen Strom for introducing him, 30 years ago, to the fascinating NGC 4486 GC system, and also the Osservatorio Astronomico di Bologna and Dr. A. Buzzoni for their hospitality during the last stages of this paper. This work was supported by grants from La Plata National University, and CONICET (PIP 712), Argentina. FF acknowledges partial financial support from the Agencia Nacional de Promoción Cienífica y Tecnológica (BID AR PICT 885).

REFERENCES

Abadi M. G., Navarro J. F., Steinmetz M., 2006, MNRAS, 365, 747
Alves-Brito A., Hau G. K.T, Forbes D. A., Spitler L. R., Strader J., Brodie J. P., Rhode K. L., 2011, MNRAS, 417, 1823
Arp H., Bertola F., 1971, ApJ, 163, 195
Bailin J., Harris W. E., 2009, ApJ, 695, 1082
Beasley M. A., Baugh C. M., Forbes D. A., Sharples R. M., Frenk C. S., 2002, MNRAS, 333, 383
Beasley M. A., Bridges T., Peng E., Harris W. E., Harris G. L. H., Forbes D. A., Mackie G., 2008, MNRAS, 386, 1443
Bekki K., Yahagi H., Nagashima M., Forbes D. A., 2008, MNRAS, 387, 1131
Bica E., Bonatto C., Barbuy B., Ortolani S., 2006, A&A, 450, 105
Bird S., Harris W. E., Blakeslee J. P., Flynn C., 2010, A&A, 524, 471
Boley A. C., Lake G., Read J., Teyssier R., 2009, ApJ, 706, 192
Brodie J. P., Strader J., 2006, AR&A, 44, 193
Bruzual G., Charlot S., 2003, MNRAS, 344, 1000
Caon N., Capaccioli M., Rampazzo R., 1990, A&AS, 86, 429
Capuzzo-Dolcetta R., Mastrobuono-Battisti A., 2009, A&A, 507, 183
Carter D., Dixon K. L., 1978, AJ, 83, 574
Chabrier G., 2003, PASP, 115, 763
Côté P., Marzke R. O., West M. J., 1998, ApJ, 501, 554
D'Onofrio M. et al., 2011, ApJ, 727, 6
Dai X., Bregman J. N., Kochaneck C. S., Rasia E., 2010, ApJ, 719, 119
de Vaoucouleurs G., Nieto J.-L., 1978, ApJ, 220, 449
Doherty M. et al., 2009, A&A, 502, 771
Durrell P. R., Harris W. E., Pritchet C. J., 2001, AJ, 121, 2557
Eggen O. J., Lynden Bell D., Sandage A. R., 1962, ApJ, 136, 748
Fabricant D., Gorestein P., 1983, ApJ, 267, 535
Faifer F. et al., 2011, MNRAS, 416, 155
Ferrarese L. et al., 2006, ApJS, 164, 334
Forbes D. A., Forte J. C., 2001, MNRAS, 322, 257
Forbes D. A., Brodie J. P., Grillmair C. J., 1997, AJ, 113, 1652
Forbes D. A., Spitler L. R., Strader J., Romanowsky A., Brodie J. P., Foster C., 2011, MNRAS, 413, 2943
Forte J. C., Strom S. E., Strom K. M., 1981, ApJ, 245, 9
Forte J. C., Martinez R.E, Muzzio J. C., 1982, AJ, 87, 1465
Forte J. C., Faifer F., Geisler D., 2005, MNRAS, 357, 56
Forte J. C., Faifer F., Geisler D., 2007, MNRAS, 382, 1947 (FFG07)
Forte J. C., Vega E. I., Faifer F., 2009, MNRAS, 397, 1003 (FVF09)
Gastaldello F., Molendi S., 2002, ApJ, 572, 160
Gebhardt K., Thomas J., 2009, ApJ, 700, 1690
Graham A. W., Guzmán R., 2003, AJ, 125, 2936
Harris W. E., 2009, ApJ, 703, 939
Harris W. E., Harris G. L. H., 2002, AJ, 123, 3108
Harris W. E., Harris G. L. H., Layden A. C., Wehner E. M. H., 2007, ApJ, 666, 903
Jones C., Stern C., Forman W., Breen J., David L., Tucker W., 1997, ApJ, 482, 143
Jordán A. et al., 2009, ApJS, 180, 54
Khochfar S., Silk J., 2009, MNRAS, 397, 506
Kim S. S., Shin J., Jin H., 2010, J. Korean Astron. Soc., 43, 105
Kissler-Patig M., 2009, in Richtler T., Larsen S., eds, Globular Clusters: Guides to Galaxies, ESO Astrophysics Symp., Springer, Berlin, Heidelberg, p. 1
Kissler-Patig M., Gebhardt K., 1998, AJ, 116, 2237
Lee M. G., Lim S., Park H. S., Hwang H. S., Hwang N., 2011, in EAS Publ. Ser. Vol. 48, A Universe of Dwarf Galaxies. EDP Sciences, Les Ulis, p. 243
Liu Ch., Peng E. W., Jordán A., Ferrarese L., Blakeslee J. P., Côté P., Mei S., 2011, ApJ, 728, 116
Liu Y., Zhou X., Ma J., Wu H., Yang Y., Li J., Chen J., 2005, AJ, 129, 2628
Mackey A. D., van den Bergh S., 2005, MNRAS, 360, 631
McLaughlin D. E., Harris W. E., Hanes D. A., 1994, ApJ, 422, 486
Maraston C., 2004, MNRAS, 363, 131
Mashchenko S., Sills A., 2005, ApJ, 619, 258
Mendel J. T., Proctor N. R., Forbes D. A., 2007, MNRAS, 379, 1618
Michard R., 2000, A&A, 360, 85
Mihos J. C., Harding P., Feldmeier J., Morrison H., 2005, ApJ, 631, 41
Miller B. W., Lotz J. M., 2007, ApJ, 670, 1074
Moyano Loyola G., Faifer F., Forte J. C., 2010, BAA&A, 53, 133
Murante G., Giovalli M., Gerhard O., Arnaboldi M., Borgani S., Dolag K., 2007, MNRAS, 377, 2
Muratov A. L., Gnedin O. Y., 2010, ApJ, 718, 1266
Murphy J. D., Gebhardt K., Adams J. J., 2011, ApJ, 729, 129
Napolitano N. R., Romanowsky A. J., Tortora C., 2010, MNRAS, 405, 2351
Norris M. et al., 2008, MNRAS, 385, 40
Oey M. S., 2000, ApJ, 542, 250
Peng E. W. et al., 2006, ApJ, 639, 838
Peng E. W. et al., 2008, ApJ, 681, 197
Peng E. W. et al., 2009, ApJ, 703, 42
Rejkuba M., Greggio L., Harris W. E., Harris G. L. H., Peng E. W., 2005, ApJ, 631, 262
Rejkuba M., Harris W. E., Greggio L., Harris G. L. H., 2011, A&A, 526, 123
Rhode K. L., Zepf S. E., Santos M. R., 2005, ApJ, 630, L21
Richtler T. et al., 2004, AJ, 127, 2094
Rudick C. S., Mihos J. C., Harding P., Feldmeier J., Janowiecki S., Morrison H. L., 2010, ApJ, 720, 569
Santos M. R., 2003, in Kissler-Patig M., ed., Extragalactic Globular Cluster Systems. Springer Verlag, New York
Schlegel D., Finkbeiner D., Davis M., 1998, ApJ, 500, 525
Schombert J., Rakos K., 2009, ApJ, 699, 1530
Schuberth Y., Richtler T., Hilker M., Dirsch B., Bassino L. P., Romanowsky A. J., Infante L., 2010, A&A, 513, 52
Searle L., Zinn R., 1978, ApJ, 225, 357
Seigar M. S., Graham A., Jerjen H., 2007, MNRAS, 378, 1575
Sérsic J. L., 1968, Atlas de Galaxias Australes, Univ. Nac. de Córdoba, Argentina
Simionescu A., Werner N., Forman W. R., Miller E. D., Takei Y., Bohringer H., Churazov E., Nulsen P. E. J., 2010, MNRAS, 405, 91

Sinnot B., Hou A., Anderson R., Harris W. E., Woodley K. A., 2011, AJ, 142, 65
Spitler L. R., 2010, MNRAS, 406, 1125
Strader J., Smith G. H., 2008, ApJ, 136, 1828
Strader J. et al., 2011, ApJS, 197, 33
Strom S. E., Forte J. C., Harris W. E., Strom K., Wells D., Smith M. G., 1981, ApJ, 245, 416
Tamura N., Sharples R. M., Arimoto N., Onodera M., Ohta K., 2006, MNRAS, 373, 601
Thomas D., Maraston C., Korn A., 2004, MNRAS, 351, L19
Tonry J. L., Dressler A., Blakeslee J. P., Ajhar E. A., Fletcher A. B., Luppino G. A., Metzger M. R., Moore C. B., 2001, ApJ, 546, 681
Tremonti C. A. et al., 2004, ApJ, 613, 898
Villegas D. et al., 2010, ApJ, 717, 603
Williams B. F. et al., 2007, ApJ, 656, 756
Worthey G., 1994, ApJ, 95, 107
Yoon S.-J., Sohn S. T., Lee S.-Y., Kim H.-S., Cho J., Chung C., Blakeslee J. P., 2011, ApJ, 743, 150
Zepf S. E., Ashman K. M., 1993, MNRAS, 264, 611
Zinn R., West M. J., 1984, ApJS, 55, 45

APPENDIX A:

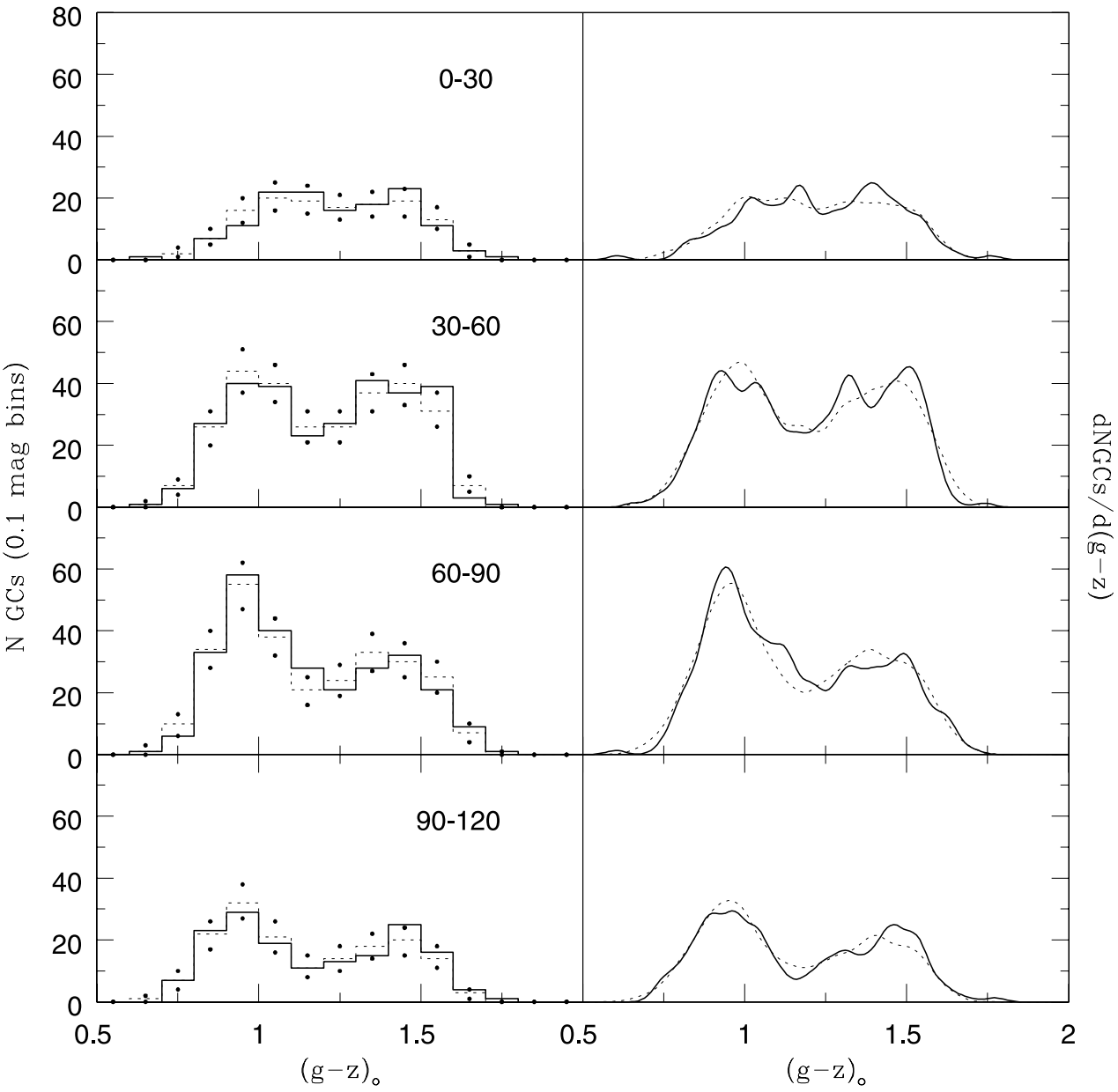

Figure A1. Left-hand panel: observed (continuous line) and model GC $(g - z)_o$ colour histograms adopting 0.1 mag bins. Dots indicate the statistical uncertainty of the model within each bin. Right-hand panel: smoothed histograms adopting a Gaussian 0.03 mag kernel. The mean semimajor axis of the annuli is given in arcsec.

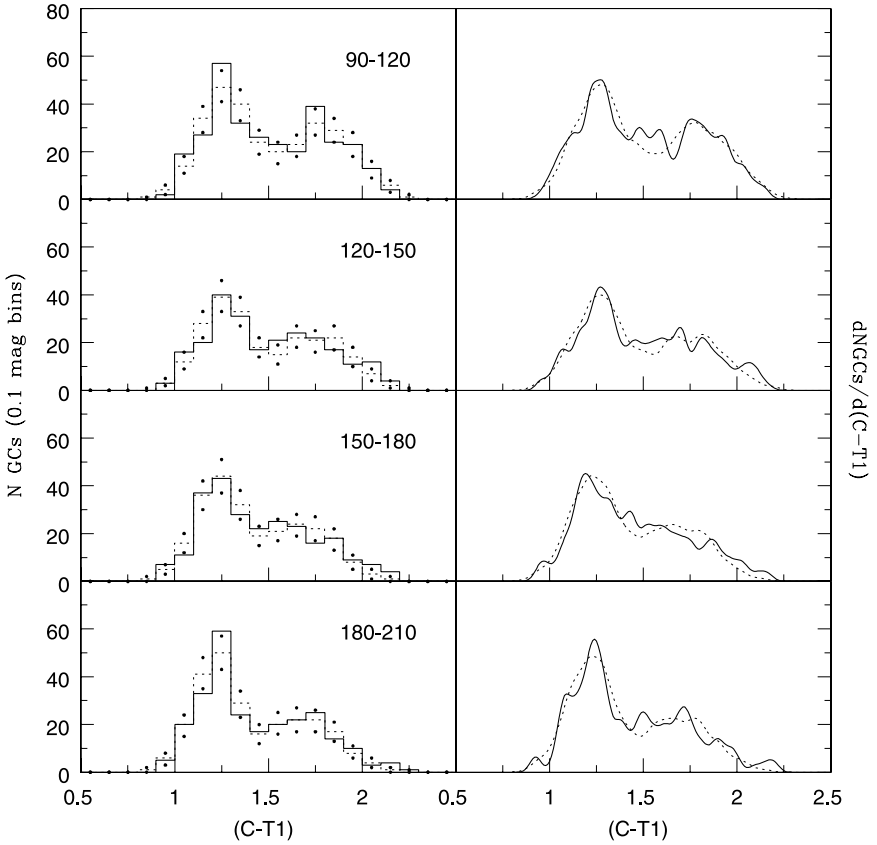

Figure A2. Left-hand panel: observed (continuous line) and model GC ($C - T_1$) colour histograms adopting 0.1 mag bins. Dots indicate the statistical uncertainty of the model within each bin. Right-hand panel: smoothed histograms adopting a Gaussian 0.03 mag kernel. The mean semimajor axis of the annuli is given in arcsec.

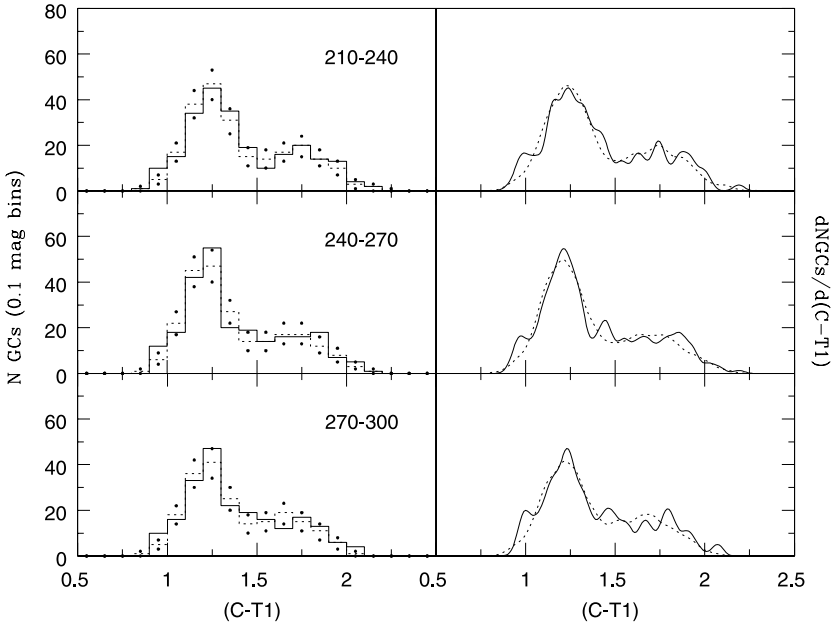

Figure A3. Left-hand panel: observed (continuous line) and model GC ($C - T_1$) colour histograms adopting 0.1 mag bins. Dots indicate the statistical uncertainty of the model within each bin. Right-hand panel: smoothed histograms adopting a Gaussian 0.03 mag kernel. The mean semimajor axis of the annuli is given in arcsec.

This paper has been typeset from a TEX/LATEX file prepared by the author.